

# Toponia at the HL-LHC, CEPC, and FCC-ee

Yang Bai<sup>a,b</sup>, Ting-Kuo Chen<sup>a</sup>, and Yiming Yang<sup>a</sup>

<sup>a</sup>*Department of Physics, University of Wisconsin-Madison, Madison, WI 53706, USA*

<sup>b</sup>*HEP Division, Argonne National Laboratory, Argonne, IL 60439, USA*

## Abstract

The discovery of a pseudoscalar toponium state at the Large Hadron Collider (LHC) opens a new avenue for the study of a novel class of QCD bound states with comparable formation and decay times. Compared to charmonium and bottomonium, toponium is a more loosely bound state, resembling a hydrogen atom of the strong interactions, although it appears as a broader resonance. We compute the masses and annihilation decay widths of the lowest  $S$ -wave ( $\eta_t, \psi_t$ ) and  $P$ -wave ( $\chi_{t0}, \chi_{t1}$ ) toponium states, and assess their discovery prospects at the High-Luminosity LHC (HL-LHC) and future lepton colliders such as the Circular Electron-Positron Collider (CEPC) and  $e^+e^-$  stage of the Future Circular Collider (FCC-ee). Detecting the vector  $\psi_t$  state at the HL-LHC is hindered by the Landau-Yang theorem and the collider's gluon-dominated nature, while lepton colliders offer discoverable sensitivity through both constituent and two-body decays. A more precise measurement of  $\eta_t$  mass—approximately equal to that of  $\psi_t$ —at the LHC could help determine the optimal  $t\bar{t}$  threshold center-of-mass energy for CEPC and FCC-ee.  $P$ -wave states remain challenging to observe at both the HL-LHC and future lepton colliders. We also discuss how we can use toponium measurements to probe top quark properties and to conduct indirect searches for new physics, including light scalars coupling to the top quark.

# Contents

<b>1</b>	<b>Introduction</b>	<b>2</b>
<b>2</b>	<b>Properties of toponium states</b>	<b>3</b>
2.1	Mass spectrum . . . . .	4
2.2	Decays . . . . .	7
2.3	Production . . . . .	9
<b>3</b>	<b>Sensitivity of toponium states at the LHC and future colliders</b>	<b>11</b>
3.1	$\eta_t$ . . . . .	12
3.2	$\psi_t$ . . . . .	13
3.3	$\chi_t$ . . . . .	16
<b>4</b>	<b>Toponium as a probe for the real singlet extension</b>	<b>16</b>
<b>5</b>	<b>Discussion and conclusions</b>	<b>19</b>
<b>A</b>	<b>Partial width formulas for the annihilation decay modes</b>	<b>20</b>
<b>B</b>	<b>Green function method for <math>P</math>-wave states</b>	<b>22</b>

# 1 Introduction

Toponium, the bound state formed by a top quark  $t$  and an anti-top quark  $\bar{t}$ , is the smallest bound state known to date in the Standard Model (SM). Characterized by a Bohr radius of  $\sim 0.01$  fm, the properties of toponia are predominantly captured by perturbative Quantum Chromodynamics (pQCD) in the short-distance regime, hence providing a novel probe for QCD properties including its asymptotic freedom behavior. Moreover, as the threshold production of  $t\bar{t}$  at lepton colliders provides an efficient way to measure the properties of the top quark, such as its mass  $m_t$  and decay width  $\Gamma_t$ , the study of the bound-state effects of toponia is crucial for the complete understanding of the SM.

The quest for toponium at colliders has long been discussed in the literature (see for example Refs. [1–9]). Recently, CMS has reported the discovery of the pseudoscalar ground state of toponium  $\eta_t$  at the Large Hadron Collider (LHC) with a significance of over  $5\sigma$  [10] via its constituent  $t$  and  $\bar{t}$  decays, which inspired several follow-up studies such as Refs. [11–13]. Fixing the top quark Monte Carlo mass  $m_t^{\text{MC}} = 172.5$  GeV and  $M_{\eta_t} = 343$  GeV (which implies a binding energy of  $E_{\text{bind}} = M_{\eta_t} - 2m_t^{\text{MC}} = -2$  GeV) in the Monte Carlo simulation, the production cross section is measured to be  $\sigma(pp \rightarrow \eta_t) = 8.8_{-1.4}^{+1.2}$  pb. This opens an avenue for the study of a novel class of QCD bound states with a bound state formation time of  $\mathcal{O}[(\alpha_s^2 m_t)^{-1}]$  that is comparable to their decay time of  $(2\Gamma_t)^{-1}$ . Because of the large top quark decay width, the toponium states behave as relatively broader resonances compared to the charmonium and bottomonium states. Furthermore, the leading discovery channel of toponium states relies on the leading constituent decay channel and not on the suppressed (with branching ratios of less than  $10^{-3}$ ) annihilation decay channels, which is opposite to the charmonium/bottomonium system.

For the discovered  $\eta_t$  state, as we will discuss more in Section 3.1, the cross section reported above has not properly taken into account the uncertainty arising from various sources, such as the renormalization scale  $\mu_R$  of the loop-corrected static QCD potential,  $m_t$ , and parton distribution function (PDF). Moreover, since the underlying simulation framework used in Ref. [10] is based on a simplified effective field theory, one can also consider improving the study using the momentum-space Green function method, which has been implemented in Ref. [14] and can be used to perform more rigorous Monte Carlo simulations. Therefore, it remains an important problem to study the properties of toponium more precisely on the theoretical side.

Because of their small relative velocity, the binding force between the constituent  $t$  and  $\bar{t}$  within a toponium system at the production threshold can be well described by the static QCD potential [15–18], with which one can solve the corresponding non-relativistic Schrödinger equation to obtain several properties of the toponium, such as its binding energy (and thus total bound-state mass) and wavefunction. Due to the large top quark decay width  $\Gamma_t = 1.42$  GeV [19], the dominant decay mode of a toponium is its intrinsic decay via the decays of individual constituents  $t$  and  $\bar{t}$ . Nevertheless, as we will discuss more in Section 3, some  $t\bar{t}$ -annihilation decay modes of a toponium can provide additional probes for other SM properties such as the top Yukawa coupling [20, 21]. To study these decays, one can use the projection method [2, 22] to isolate the partial-wave toponium state of interest, which can also be used to study the production of toponia at colliders. However, since the projection method does not take into account the interplay between the continuous  $t\bar{t}$  and bound-state toponium production mechanisms, certain quantities (such as the differential cross section  $d\sigma/dm_{t\bar{t}}$ ,  $m_{t\bar{t}}$  being the

invariant mass of the  $t\bar{t}$  system) must be computed by other methods. For example, the Green function method [1, 4, 7–9, 23, 24] makes use of the optical theorem to incorporate bound-state effects into the continuous spectrum. As we show later, these two methods give comparable  $pp \rightarrow \eta_t$  cross sections that are also consistent with the CMS measurement reported in Ref. [10], which allows the use of the projection method for our purpose of surveying the sensitivity of several toponium states at the current LHC and other future colliders.

As mentioned earlier, since the study of toponia is crucial for the complete understanding of the SM, it is of great importance to survey other possible search channels than the  $pp \rightarrow \eta_t \rightarrow bW^+\bar{b}W^-$  process at the current LHC. For example, in this study, we find that the  $\eta_t b\bar{b}$  production can already be sensitive at the 13-TeV LHC, while the  $\eta_t \rightarrow ZH$  decay could be significant enough at the High-Luminosity LHC (HL-LHC) [25] if the  $ZH$  final state can be efficiently reconstructed and distinguished from the background. On the other hand, although it is difficult for  $\eta_t$  to be directly produced at lepton colliders due to its  $J^{PC}$  quantum numbers,  $\psi_t$  turns out to be a fairly promising state to be probed at these facilities, which has been pointed out for long in the literature (see for example Refs. [23, 26–28]). On the contrary, the direct production of  $gg \rightarrow \psi_t$  is prohibited by the Landau-Yang theorem [29, 30], and thus it is challenging to discover  $\psi_t$  at hadron colliders. In this study, we especially discuss the Circular Electron-Positron Collider (CEPC) [31, 32] and the  $e^+e^-$  stage of the Future Circular Collider (FCC-ee) [33–35], both of which propose to run around the  $t\bar{t}$  threshold with an integrated luminosity of  $\mathcal{O}(1) \text{ ab}^{-1}$ . For  $\psi_t$ , in addition to the individual  $t$  and  $\bar{t}$  decays, Ref. [12] shows that its leading  $t\bar{t}$ -annihilation decay to  $b\bar{b}$  can also be probed via some specially designed observable that captures the interference with the  $\gamma$ - and  $Z$ -mediated processes caused by the  $\psi_t$  mass pole. Moreover, similar to the case of  $\eta_t \rightarrow ZH$ , one can also possibly probe the  $e^+e^- \rightarrow \psi_t \rightarrow \gamma H$  process if the final-state signals can be efficiently extracted.

Finally, in addition to probing the SM, one can also constrain certain beyond-SM (BSM) physics with toponium measurements, such as new scalar fields that either affect the top Yukawa coupling of the 125-GeV Higgs boson or contribute additional Yukawa interactions to the static toponium QCD potential. In our study, we use the  $\mathbb{Z}_2$ -symmetric real-singlet extension to the SM (SSM) as an example and show how the  $\eta_t$  measurement performed in Ref. [10] can be used to constrain its parameter space, while one can certainly generalize this idea to other BSM models.

Our paper is organized as follows. In Section 2, we review the theoretical properties of toponia, including their masses, decays, and production at colliders, with the details of the  $t\bar{t}$ -annihilation decay formulas and the results of  $P$ -wave Green function calculation summarized in Appendices A and B, respectively. In Section 3, we discuss the discovery sensitivity of the four toponium states  $\eta_t$ ,  $\psi_t$ ,  $\chi_{t0}$ , and  $\chi_{t1}$  at the current LHC and future HL-LHC, CEPC, and FCC-ee. In Section 4, we perform a parameter space study on the SSM using the  $\eta_t$  measurement conducted by CMS as an example of probing BSM physics using toponium. Finally, we conclude our study in Section 5.

## 2 Properties of toponium states

In this section, we summarize some basic properties of the toponium states, including their mass spectrum, decays, and production at colliders.

## 2.1 Mass spectrum

The binding energy and wavefunction of a heavy quarkonium near the threshold can be obtained by solving the non-relativistic Schrödinger equation given the small velocities of the constituent quarks. For a color-singlet toponium system in the short-distance regime, the associated static potential described by pQCD up to two-loop is given by [9, 15–19]

$$V_{\text{pQCD}}(r) = -\frac{C_F \alpha_s(\mu_R)}{r} \left\{ 1 + \frac{\alpha_s(\mu_R)}{4\pi} [a_1 + 2\gamma_E \beta_0] \right. \\ \left. + \left( \frac{\alpha_s(\mu_R)}{4\pi} \right)^2 \left[ a_2 + \left( \frac{\pi^2}{3} + 4\gamma_E^2 \right) \beta_0^2 + 2\gamma_E (2a_1 \beta_0 + \beta_1) \right] \right\}, \quad (2.1)$$

where  $\gamma_E \approx 0.577$  is the Euler-Mascheroni constant and  $\alpha_s(\mu_R)$  is the strong coupling at the renormalization scale  $\mu_R$  as given by

$$\alpha_s(\mu_R) = \frac{4\pi}{\beta_0 \log(\mu_R^2/\Lambda^2)} \left\{ 1 - \frac{\beta_1 \log[\log(\mu_R^2/\Lambda^2)]}{\beta_0^2 \log(\mu_R^2/\Lambda^2)} \right\}. \quad (2.2)$$

A convenient scale choice of  $\mu_R$  is  $\sim 1/r$ , which we will stick to in this study and check the related variation later. The color  $SU(3)$  group constants are defined through  $C_F = 4/3$ ,  $C_A = 3$ ,  $T_F = 1/2$ ,  $n_f = 5$ ,  $\beta_0 = 11C_A/3 - 4T_F n_f/3$ ,  $\beta_1 = 34C_A^2/3 - 20C_A T_F n_f/3 - 4C_F T_F n_f$ , and

$$a_1 = \frac{31}{9}C_A - \frac{20}{9}T_F n_f, \quad (2.3)$$

$$a_2 = \left[ \frac{4343}{162} + 4\pi^2 - \frac{\pi^4}{4} + \frac{22}{3}\zeta(3) \right] C_A^2 - \left[ \frac{1798}{81} + \frac{56}{3}\zeta(3) \right] C_A T_F n_f \\ - \left[ \frac{55}{3} - 16\zeta(3) \right] C_F T_F n_f + \left[ \frac{20}{9}T_F n_f \right]^2. \quad (2.4)$$

In the long-distance regime, one can replace the potential in Eq. (2.1) with the Cornell potential

$$V_{\text{Cornell}} = -\frac{C_F \alpha_s^{\text{Cornell}}}{r} + b r, \quad (2.5)$$

starting from the transition point  $r = r_0 = 0.1$  fm, where  $\alpha_s^{\text{Cornell}} = 0.211$  and  $b = 0.212$  GeV<sup>2</sup> are taken to be fixed values evaluated at the transition point (see Ref. [36] for the results from Lattice QCD calculations). Overall, one has the complete static potential

$$V_{\text{static}}(r) = \begin{cases} V_{\text{pQCD}}(r) & , \quad r \leq r_0 \\ V_{\text{Cornell}}(r) & , \quad r > r_0 \end{cases}. \quad (2.6)$$

Note that the Bohr radius of the toponium states  $a_t$  can be estimated using the Coulomb potential as  $a_t = (C_F \alpha_s m_t/2)^{-1} \sim (18 \text{ GeV})^{-1}$ . One then has  $\alpha_s = \alpha_s(a_t^{-1}) \approx \alpha_s(18 \text{ GeV}) \approx 0.157$  and  $a_t \approx 0.011$  fm [19], which is one order of magnitude smaller than the transition radius  $r_0$ . This also means that the properties of toponia are dominated by the short-distance pQCD potential.

To calculate the mass splitting among the different toponium states with the same orbital angular momentum, one can use the spin-dependent potential [37]

$$V_{\text{spin-dep}}(r) = \frac{8\alpha_s(\mu_R)}{9m_t^2 r^2} \delta(r) \vec{S}_t \cdot \vec{S}_{\bar{t}} + \frac{1}{m_t^2} \left[ \left( \frac{2\alpha_s(\mu_R)}{r^3} - \frac{b}{2r} \right) \vec{L} \cdot \vec{S} + \frac{4\alpha_s(\mu_R)}{r^3} \mathbb{T} \right]. \quad (2.7)$$

Here,  $\vec{S}_t$  and  $\vec{S}_{\bar{t}}$  are the spin operators of the top and anti-top quarks, respectively.  $\vec{S} = \vec{S}_t + \vec{S}_{\bar{t}}$  is the total spin angular momentum operator,  $\vec{L}$  is the orbital angular momentum operator, and  $\vec{J} = \vec{S} + \vec{L}$  is the total angular momentum operator. We denote  $S, L, J$  as the eigenvalues of the corresponding angular momentum operators. The tensor operator  $\mathbb{T}$  has non-zero eigenvalues only between the  $L > 0$  spin-triplet states as

$$\langle {}^3L_J | \mathbb{T} | {}^3L_J \rangle = \begin{cases} -\frac{L}{6(2L+3)} & , \quad J = L + 1 \\ +\frac{1}{6} & , \quad J = L \\ -\frac{L+1}{6(2L-1)} & , \quad J = L - 1 \end{cases}. \quad (2.8)$$

toponium	binding energy [GeV]		$R_S(0) [a_t^{-3/2}]$ ,	$R'_P(0) [a_t^{-5/2}]$
	$m_t = 172.4 \pm 0.7$ GeV	$\mu_R = (1.0^{+1.0}_{-0.5})/r$	$m_t$	$\mu_R$
<i>S</i> -wave	$-2.725^{+0.005}_{-0.005}$	$-2.725^{+0.654}_{-1.020}$	$1.611^{+0.001}_{-0.001}$	$1.611^{+0.235}_{-0.205}$
<i>P</i> -wave	$-1.375^{+0.003}_{-0.003}$	$-1.375^{+0.430}_{-0.813}$	$0.2346^{+0.0003}_{-0.0003}$	$0.2346^{+0.0208}_{-0.0444}$

Table 1: The binding energies and (derivatives of) the radial wavefunctions at the origin for the lowest *S*-wave and *P*-wave toponium states obtained by solving the Schrödinger equation with the full  $V_{\text{static}}(r)$  given in Eq. (2.6). The uncertainties come either from the experimental uncertainty in  $m_t$  or the variation of the renormalization scale  $\mu_R$  from  $0.5/r$  to  $2/r$ .

By solving the Schrödinger equation with the full static potential given in Eq. (2.6), one can obtain the binding energy  $E_{\text{bind}}$  (which can be either positive or negative) and wavefunction of a given toponium state. The bound-state mass of a toponium is then given by  $M = 2m_t + E_{\text{bind}}$ , where the top quark mass is taken to be the measured pole mass  $m_t = m_t^{\text{pole}} = 172.4 \pm 0.7$  GeV [19]. The uncertainty in  $m_t$  will introduce an uncertainty in the toponium mass of around  $\delta M \approx 1.4$  GeV. Moreover, since there is no definitive way to fix  $\mu_R$ , the range of this choice will lead to an additional uncertainty of  $\mathcal{O}(1 \text{ GeV})$  in  $\delta M$  through  $\alpha_s(\mu_R)$ , which can be seen in Table 1, in which we investigated the binding energies and the values at the origin of the wavefunctions  $R_S(r)$  [the derivatives of wavefunctions  $R'_P(r)$ ] for the *S*-wave (*P*-wave) states, respectively, by varying  $\mu_R$  from  $0.5/r$  to  $2/r$ . Overall, the uncertainty in the predicted toponium mass is  $\delta M \simeq 2$  GeV. Using the obtained wavefunctions and Eq. (2.7), we calculate the mass splittings among the states with the same  $L$  and show the spectrum of the first few *S*- and *P*-wave states in Figure 1, where we fix the top quark mass  $m_t$  at its central value 172.4 GeV and the renormalization scale  $\mu_R = 1/r$ . Note that all toponia have an uncertainty of around  $\delta M \sim 2$  GeV coming from the uncertainties in  $m_t$  and  $\mu_R$  as mentioned previously, while the relative mass differences are all much smaller and thus negligible.

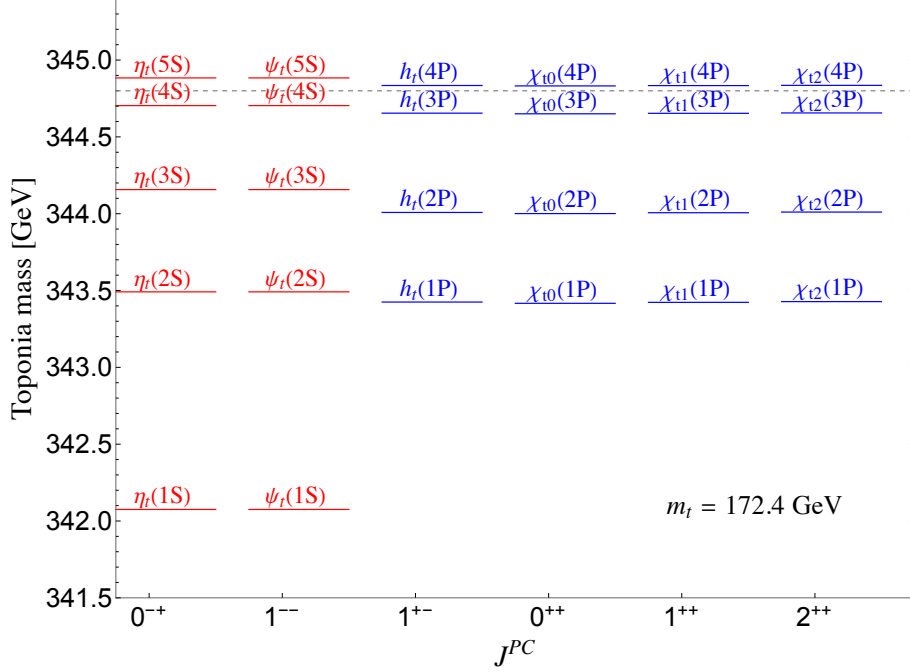


Figure 1: The mass spectrum of the lowest  $S$ - and  $P$ -wave toponium states, categorized by their principal quantum number  $n$  and  $n - 1$  and  $J^{PC}$  quantum numbers. In this plot, we fix  $m_t = 172.4$  GeV, and the gray dashed line denotes the threshold mass  $2m_t = 344.8$  GeV, above and below which  $E_{\text{bind}} > 0$  and  $E_{\text{bind}} < 0$ , respectively. The renormalization scale for  $\alpha_s(\mu_R)$  in the static potential is chosen to be  $\mu_R = 1/r$ . There is an uncertainty of around  $\delta M \sim 2$  GeV for all toponium masses resulting from the top quark mass and renormalization scale uncertainties. The mass difference between  $\eta_t(nS)$  and  $\psi_t(nS)$  is negligible and that among the  $P$ -wave states with the same principle quantum number  $n - 1$  is around 5 MeV. On the other hand, the mass splitting between  $S$ - and  $P$ -wave states with the same principle quantum number  $n$  is sizable, *e.g.*, the mass difference between  $\eta_t(2S)$  and  $h_t(1P)$  is 66 MeV.

Note that because  $\alpha_s(a_t^{-1})/\pi \approx 0.05 \ll 1$  for a typical toponium system, it can be well described by pQCD through the leading-order Coulomb potential  $V_{\text{Coul}}(r) = -C_F \alpha_s^{\text{Coul}}/r$ , where  $\alpha_s^{\text{Coul}}$  is a fixed number whose value we will determine later, with both the loop correction and linear potential neglected. Likewise, the other  $S, L, J, T$ -dependent terms are subdominant compared to  $V_{\text{Coul}}$  and will only produce small splittings among the masses of the different toponium states, which we label using the term symbol  $^{2S+1}L_J$ . As a result, as far as the wavefunctions of the different toponium states are concerned, taking  $V \approx V_{\text{Coul}}$  is in general a good approximation. To demonstrate this, we fix  $\alpha_s^{\text{Coul}}$  by matching the derived binding energy of the  $S$ -wave states to that calculated from using the full  $V_{\text{static}}(r)$  given in Eq. (2.6). This matching leads to  $\alpha_s^{\text{Coul}} = 0.189$ . We then compare the values of the radial wavefunctions of the two lowest  $S$ -wave states  $\eta_t(^1S_0), \psi_t(^3S_1)$  [ $R_S(r)$ ] and the derivatives of those of the two lowest  $P$ -wave states  $\chi_{t0}(^3P_0), \chi_{t1}(^3P_1)$  [ $R'_P(r)$ ] at the origin  $r = 0$  using both  $V_{\text{Coul}}(r)$  and the full

$V_{\text{static}}(r)$ . We list the latter in Table 1, while the former are given by

$$R_S(0) = 2 \left( \frac{4 \alpha_s^{\text{Coul}} m_t}{3} \right)^{\frac{3}{2}} = 2(a_t^{\text{Coul}})^{-\frac{3}{2}}, \quad R'_P(0) = \frac{1}{\sqrt{24}} \left( \frac{4 \alpha_s^{\text{Coul}} m_t}{3} \right)^{\frac{5}{2}} \approx 0.2041(a_t^{\text{Coul}})^{-\frac{5}{2}}, \quad (2.9)$$

with the binding energies of the  $P$ -wave states being  $-0.6812$  GeV. One can see that the two methods indeed give close though not identical results. This discrepancy can be explained by the following reasons. First, when  $r \rightarrow 0$ , the full potential  $V_{\text{static}}$  will be suppressed through the running of  $\alpha_s(\mu_R \sim 1/r)$  due to the asymptotic freedom of QCD, while  $V_{\text{Coul}}$  remains parametrized by the fixed  $\alpha_s^{\text{Coul}}$ . This difference between the behavior of the two potentials at short distance will then influence (the derivative) of the wavefunctions at the origin. Second, the  $P$ -wave wavefunctions are distributed considerably about  $r \sim \mathcal{O}(1)a_t$ , which causes them to receive more corrections from the long-distance contribution of the static potential compared to the  $S$ -wave states. We further scan  $\kappa \equiv \mu_R \times r$  and find that the larger  $\kappa$ , the more similar the  $S$ -wave wavefunctions derived with  $V_{\text{static}}$  and  $V_{\text{Coul}}$  will be. This is because  $\alpha_s(\mu_R = \kappa/r)$  will decrease along with shorter  $r$ , making the system more similar to the case described only by  $V_{\text{Coul}}$ , which after matching  $E_{\text{bind}} = -1.88$  GeV is parametrized by  $\alpha_s = \alpha_s(a_t^{-1}) = 0.157$ . In the remainder of the study, we will only use  $V_{\text{Coul}}$  with  $\alpha_s^{\text{Coul}} = 0.189$  to calculate the wavefunctions for simplification, which we will discuss more in Section 3.1.

## 2.2 Decays

The dominant decay mode of toponia is the intrinsic decays of the constituent top and anti-top quarks with the decay width  $\Gamma \approx \Gamma_t + \Gamma_{\bar{t}} = 2\Gamma_t = 2.84$  GeV [19]. On top of that, one can also consider the  $t\bar{t}$ -annihilation decay modes, which have been considered in Refs. [2, 22] and calculated using the ‘‘projection method’’, which works as follows: Consider a generic  $Q\bar{Q} \rightarrow f$  annihilation process with the matrix element

$$\mathcal{M}(Q\bar{Q} \rightarrow f) = \bar{v}^s \left( \frac{p}{2} - q \right) \mathcal{O}(p, q) u^{s'} \left( \frac{p}{2} + q \right), \quad (2.10)$$

from which we further define  $\mathcal{O}(0) \equiv \mathcal{O}(p, q = 0)$  and  $\mathcal{O}^\alpha(0) \equiv \frac{\partial}{\partial q_\alpha} \mathcal{O}(p, q)|_{q=0}$ . Consequently, one can write down the bound-state version of the matrix element  $\mathcal{M}[B^{(2S+1)L_J} \rightarrow f] \equiv \mathcal{A}^{(2S+1)L_J}$  in the non-relativistic limit, where  $B^{(2S+1)L_J}$  is the  $Q\bar{Q}$  bound state characterized by the quantum numbers  $S, L, J$ . For the  $S$ -wave states, one has

$$\mathcal{A}^{(1S_0)} = \frac{1}{\sqrt{3}} \frac{1}{\sqrt{M_B}} \frac{1}{2} \frac{1}{\sqrt{4\pi}} R_S(0) \text{Tr}[\mathcal{O}(0)(M_B + \not{p})(-\gamma^5)], \quad (2.11)$$

$$\mathcal{A}^{(3S_1)} = \frac{1}{\sqrt{3}} \frac{1}{\sqrt{M_B}} \frac{1}{2} \frac{1}{\sqrt{4\pi}} R_S(0) \text{Tr}[\mathcal{O}(0)(M_B + \not{p})(-\gamma^\mu)] \varepsilon_\mu(p), \quad (2.12)$$

where  $\varepsilon_\mu(p)$  is the polarization vector of the  $^3S_1$  state, which is the  $\psi_t$  state when it comes to toponium. Note that the trace is also taken over the color indices, while the prefactor  $\frac{1}{\sqrt{3}}$  arises from the projection onto the color-singlet component of the  $t\bar{t}$  bound state. As for the  $P$ -wave states, one has

$$\mathcal{A}^{(1P_1)} = \frac{1}{\sqrt{3}} \frac{i}{\sqrt{M_B}} \frac{1}{2} \sqrt{\frac{3}{4\pi}} R'_P(0) \text{Tr} \left[ \left[ \mathcal{O}^\mu(0) - \frac{2}{M_B} \mathcal{O}(0) \gamma^\mu \right] (M_B + \not{p}) \gamma^5 \right] \varepsilon_\mu(p), \quad (2.13)$$

$$\mathcal{A}(^3P_0) = \frac{1}{\sqrt{3}} \frac{i}{\sqrt{M_B}} \sqrt{\frac{1}{4\pi}} R'_P(0) \text{Tr} \left[ \frac{1}{2} \mathcal{O}^\mu(0) (\gamma_\mu + \frac{p_\mu}{M_B}) (\not{p} - M_B) + 3\mathcal{O}(0) \right], \quad (2.14)$$

$$\mathcal{A}(^3P_1) = \frac{1}{\sqrt{3}} \frac{1}{\sqrt{M_B}} \sqrt{\frac{3}{8\pi}} R'_P(0) \epsilon_{\alpha\beta\gamma\delta} \frac{p^\gamma}{M_B} \text{Tr} \left[ \frac{1}{2} \mathcal{O}^\alpha(0) \gamma^\beta (\not{p} - M_B) - \mathcal{O}(0) \gamma^\alpha \gamma^\beta \frac{\not{p}}{M_B} \right] \varepsilon^\delta(p), \quad (2.15)$$

$$\mathcal{A}(^3P_2) = \frac{1}{\sqrt{3}} \frac{i}{\sqrt{M_B}} \frac{1}{2} \sqrt{\frac{3}{4\pi}} R'_P(0) \text{Tr} [\mathcal{O}^\alpha(0) \gamma^\beta (\not{p} - M_B)] \varepsilon_{\alpha\beta}(p). \quad (2.16)$$

Later in this study, we will focus on the phenomenology of  $\eta_t$ ,  $\psi_t$ ,  $\chi_{t0}$ , and  $\chi_{t1}$ , the branching ratios of whose annihilation decay modes are summarized in Table 2 with the detailed corresponding formulas listed in Appendix A (see also Refs. [3, 38]). Here we take the massless limits for the fermions, and thus the fermionic decay modes of  $\eta_t$  and  $\chi_{t0}$ , whose couplings to fermion pairs are proportional to the fermions masses, become negligible, with the exception of the  $\eta_t \rightarrow b\bar{b}$  decay, for which we retain the non-zero bottom quark mass during the calculation. Note that all annihilation decay modes have partial widths that are significantly smaller than the intrinsic decay width  $\Gamma$ , and some of them are prohibited by  $J^{PC}$  conservation and thus have exactly zero partial widths. We will discuss the sensitivity of toponium states in some of these channels at the LHC and future colliders in Section 3.

decay mode (branching ratio)	$\eta_t$ ( $0^{-+}$ )	$\psi_t$ ( $1^{--}$ )	$\chi_{t0}$ ( $0^{++}$ )	$\chi_{t1}$ ( $1^{++}$ )
$W^+W^-$	$2.42 \times 10^{-4}$	$9.96 \times 10^{-4}$	$1.28 \times 10^{-6}$	$1.45 \times 10^{-6}$
$ZZ$	$1.22 \times 10^{-5}$	$9.29 \times 10^{-6}$	$1.70 \times 10^{-7}$	$1.47 \times 10^{-8}$
$ZH$	$1.02 \times 10^{-3}$	$1.38 \times 10^{-5}$	0	$9.84 \times 10^{-7}$
$HH$	0	0	$4.34 \times 10^{-6}$	0
$\gamma\gamma$	$1.78 \times 10^{-5}$	0	$2.65 \times 10^{-8}$	0
$\gamma H$	0	$1.14 \times 10^{-4}$	0	0
$\gamma Z$	$3.94 \times 10^{-6}$	$1.32 \times 10^{-4}$	$6.47 \times 10^{-9}$	$1.15 \times 10^{-10}$
$\nu\bar{\nu}$	-	$1.30 \times 10^{-6}$	-	$8.62 \times 10^{-9}$
$\ell^+\ell^-$	-	$1.45 \times 10^{-5}$	-	$4.34 \times 10^{-9}$
$u\bar{u}, c\bar{c}$	-	$2.47 \times 10^{-5}$	-	$1.49 \times 10^{-8}$
$d\bar{d}, s\bar{s}$	-	$1.14 \times 10^{-5}$	-	$1.91 \times 10^{-8}$
$b\bar{b}$	$7.36 \times 10^{-8}$	$8.54 \times 10^{-4}$	-	$3.34 \times 10^{-8}$
$gg$	$4.58 \times 10^{-3}$	0	$6.81 \times 10^{-6}$	0
$ggg$	0	$2.77 \times 10^{-5}$	0	0

Table 2: The branching ratios of the  $t\bar{t}$ -annihilation decay modes of  $\eta_t$ ,  $\psi_t$ ,  $\chi_{t0}$ , and  $\chi_{t1}$ . Some decay modes are prohibited by  $J^{PC}$  conservation and thus have exactly zero partial widths. Here we ignore the fermion masses, and thus the fermionic decay widths of  $\eta_t$  and  $\chi_{t0}$  are negligible, denoted as “-”, except for  $\eta_t \rightarrow b\bar{b}$ , for which we explicitly include the non-zero bottom quark mass in the calculation. For the results with non-zero fermion masses, we refer to Refs. [3, 38].

## 2.3 Production

To calculate the production cross sections of toponia, one can use the projection method by modifying the kinematics accordingly and then applying the same formulas as in Eqs. (2.11)-(2.16). For example, the gluon fusion production cross section of an exactly on-shell  $\eta_t$  at the parton level is given by

$$\hat{\sigma}(gg \rightarrow \eta_t)_{\text{on-shell}} = \frac{\pi^2 \alpha_s^2}{3M\hat{s}} |R_S(0)|^2 \delta(\hat{s} - M^2), \quad (2.17)$$

where  $\sqrt{\hat{s}}$  is the parton-level center-of-mass energy. Alternatively, one can also include the finite-width effect by using the Breit-Wigner (B-W) formula, which gives

$$\hat{\sigma}(gg \rightarrow \eta_t)_{\text{B-W}} = \frac{\pi \alpha_s^2}{3M^2 \Gamma \hat{s}} |R_S(0)|^2 \frac{\Gamma^2/4}{(\sqrt{\hat{s}} - M)^2 + \Gamma^2/4}. \quad (2.18)$$

In general, the projection method is an appropriate way to compute processes involving bound states, as long as the magnitude of the relative momentum between the constituent quarks  $|\vec{q}|$  is much smaller than the bound-state mass  $M$ , which is usually the case in reality for the production of heavy quarkonia near the threshold [39]. For simplicity, we will use this method to estimate the production cross sections in the sensitivity study in Section 3.

Nevertheless, the projection method ignores the interplay between the continuous  $t\bar{t}$  and bound-state toponium production mechanisms, which is important when it comes to scrutinizing the differential cross sections constructed from measuring their identical decay products. To incorporate this interplay into the calculations, one can turn to the ‘‘Green function method’’ [1, 7–9, 23, 24], which is based on the optical theorem and accounts for the enhancement near the threshold by multiplying the continuous production cross section by the ratio of the imaginary part of the bound-state Green function to that of the free Green function. For instance, the gluon fusion production cross section of  $bW^+\bar{b}W^-$  through the  $S$ -wave color-singlet toponium states can be calculated via [7, 9]

$$\hat{\sigma}(gg \rightarrow t\bar{t} \rightarrow bW^+\bar{b}W^-)_S = \hat{\sigma}(gg \rightarrow t\bar{t} \rightarrow bW^+\bar{b}W^-)_{S,\text{tree}} \frac{\text{Im}[G(r, E)]_{r=0}}{\text{Im}[G_0(r, E)]_{r=0}}, \quad (2.19)$$

where  $\sigma_{S,\text{tree}}$  is the Born-level continuous production cross section through on-shell  $t\bar{t}$ , and  $G_0$  and  $G$  denote the free and bound-state Green functions of the  $t\bar{t}$  system, respectively. The bound-state Green function  $G$  is solved from the following Schrödinger equation,<sup>1</sup>

$$\left[ \frac{\nabla^2}{m_t} - V(r) + z \right] G(\vec{r}, z) = \delta^3(\vec{r}), \quad z = E + i\Gamma_t, \quad (2.20)$$

where we approximate the QCD potential  $V(r) \approx V_{\text{Coul}}(r) = -C_F \alpha_s^{\text{Coul}}/r$ . The analytic solution to Eq. (2.20) is given by [41]

$$G(r, E) = \frac{m_t^2}{4\pi} a \Gamma \left( -\frac{ia}{2\sqrt{z'}} \right) e^{i\sqrt{z'}\rho} U \left( 1 - \frac{ia}{2\sqrt{z'}}, 2, -2i\sqrt{z'}\rho \right), \quad (2.21)$$

<sup>1</sup>One can also apply the Green function method in the momentum space as studied in Refs. [14, 40], which is useful for Monte Carlo simulations of kinematic observables.

where we use the dimensionless quantities  $\rho = m_t r$ ,  $z' = z/m_t$ , and  $a = C_F \alpha_s^{\text{Coul}}$ . Here,  $\Gamma(x)$  is the gamma function and  $U(\mathbf{a}, \mathbf{b}, x)$  is the Tricomi confluent hypergeometric function. When  $a \rightarrow 0$ , one retrieves the free Green function  $G_0$ ,

$$G_0(r, E) = -\frac{m_t^2 e^{i\sqrt{z'}\rho}}{4\pi \rho}. \quad (2.22)$$

When  $r \rightarrow 0$ ,  $G$  has an asymptotic behavior,

$$\lim_{r \rightarrow 0} G(r, E) \rightarrow \frac{m_t^2}{4\pi} \left[ -\frac{1}{\rho} + a \log \rho - 2ia\pi + a \log(-2i\sqrt{z'}) \right. \\ \left. + \psi^{(0)} \left( 1 - \frac{ia}{2\sqrt{z'}} \right) + 2\gamma_E a - a - i\sqrt{z'} \right], \quad (2.23)$$

where  $\psi^{(n)}(x)$  is the  $n$ -th derivative of the digamma function. Consequently, one can define the  $S$ -wave Sommerfeld enhancement factor as

$$\mathcal{S}_S(E) \equiv \frac{\text{Im}[G(r, E)]_{r=0}}{\text{Im}[G_0(r, E)]_{r=0}} = \frac{\text{Im} \left[ -a \log(-2i\sqrt{z'}) - a \psi^{(0)} \left( 1 - i\frac{a}{2\sqrt{z'}} \right) + i\sqrt{z'} \right]}{\text{Im} [i\sqrt{z'}]}. \quad (2.24)$$

It is worth noting that the denominator in Eq. (2.24) will in general cancel the kinematic factor  $\sqrt{1 - 4m_t^2/\hat{s}}$  in the cross section formula when  $\Gamma_t \rightarrow 0$ , allowing us to extend the distribution of differential cross section  $d\sigma/dm_{t\bar{t}}$  below the threshold of  $2m_t$  without inducing an imaginary number, as shown in Ref. [24].

Here we demonstrate the consistency between the Green function and projection methods regarding the production cross section of the process  $pp \rightarrow \eta_t$ . For the Green function method, we take  $V_{\text{Coul}}(r)$  with  $\alpha_s^{\text{Coul}} = 0.189$  as obtained from matching the  $S$ -wave binding energy with  $\mu_R = 1/r$  in Section 2.1, while for the projection method, we use the same setup as in Section 2.2 when studying the annihilation decays and adopt the B-W formula. We compute the differential cross section  $d\sigma(pp \rightarrow \eta_t)/dm_{t\bar{t}}$  with both methods and show the two results in Figure 2. One can see that the two methods give fairly different curves, which is a result of their different treatments of the interference between the bound-state and continuous  $t\bar{t}$  systems, as mentioned previously [9]. Next, we define the ‘‘resonance’’ region of the  $t\bar{t}$  invariant mass to be  $m_{t\bar{t}} \in [M_{\eta_t} - \Gamma, M_{\eta_t} + \Gamma] = [342.08 - 2.84, 342.08 + 2.84]$  GeV and integrate the differential cross section over this interval to obtain the proton-level production cross section  $\sigma(pp \rightarrow \eta_t)_{\text{Green}} = 7.08$  pb, which is compatible with the experimental result of  $\sigma(pp \rightarrow \eta_t) = 8.8_{-1.4}^{+1.2}$  pb reported in Ref. [10] within  $2\sigma$ . On the other hand, the projection method gives the cross section of  $\sigma(pp \rightarrow \eta_t)_{\text{Projection}} = 6.89$  pb, which is also compatible with both the Green function and the experimental results. Note that the  $K$ -factor is very close to one and thus does not influence the results here much, as mentioned in Ref. [9]. Moreover, the differential cross section derived from the Green function method is only reliable around the  $m_{t\bar{t}} = 2m_t$  threshold, where the non-relativistic assumption made in Eq. (2.20) is justified. To extend the applicable window to larger  $m_{t\bar{t}}$ , we refer to Ref. [9]. In general, one can also generalize the Green function method to the  $P$ -wave case; however, as we will demonstrate in Section 3.3, the production cross sections of  $P$ -wave toponia at future colliders are too small to be sensitive to experimental searches, and thus we only present the corresponding comparison in Appendix B.

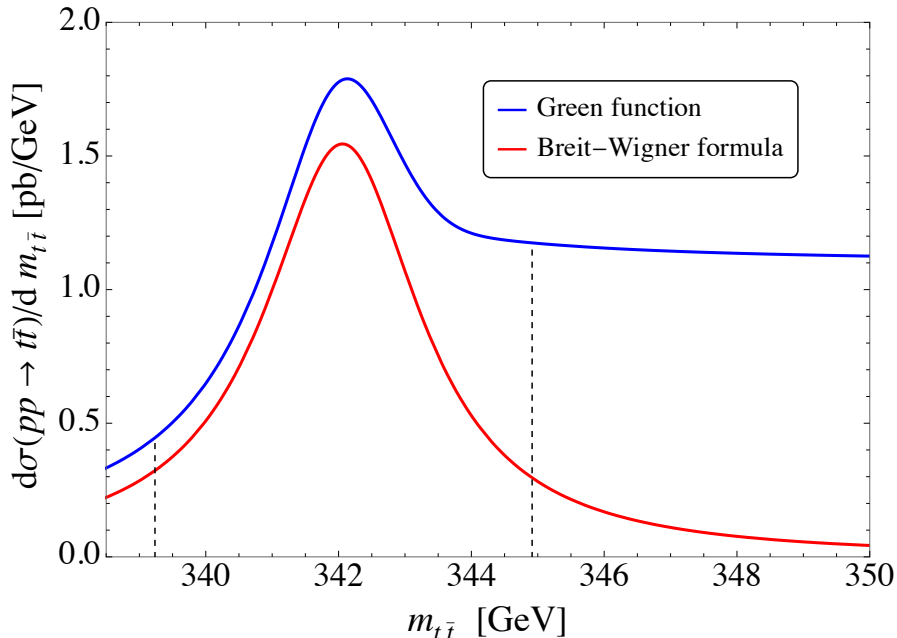


Figure 2: The  $d\sigma(pp \rightarrow \eta_t)/dm_{t\bar{t}}$  distributions at the 13-TeV LHC calculated using the leading-order Green function method (blue) and the B-W formula (red). The two dashed lines represent  $m_{t\bar{t}} = M_{\eta_t} \pm \Gamma$  with  $M_{\eta_t} = 342.08$  GeV and  $\Gamma = 2.84$  GeV, respectively, between which we identify the  $t\bar{t}$  system to be on “resonance”.

### 3 Sensitivity of toponium states at the LHC and future colliders

In this section, we discuss the discovery sensitivity of  $\eta_t$ ,  $\psi_t$ ,  $\chi_{t0}$ , and  $\chi_{t1}$  at the LHC and future colliders, including the HL-LHC, CEPC, and FCC-ee. For the associated annihilation decays and production cross sections, we calculate them using the projection method reviewed in Sections 2.2 and 2.3 and ignore the  $K$ -factors. A brief summary of the proposed specs of the future colliders mentioned is given in Table 3.

future collider	$\sqrt{s}$	expected integrated luminosity ( $\mathcal{L}$ )
HL-LHC	14 TeV	3 ab <sup>-1</sup>
CEPC	360 GeV	1 ab <sup>-1</sup>
FCC-ee	360 GeV	2.70 ab <sup>-1</sup>
	340-350 GeV	0.42 ab <sup>-1</sup>

Table 3: A brief summary of the proposed specs of the HL-LHC [25], CEPC [31, 32], and FCC-ee [34, 35].

### 3.1 $\eta_t$

We begin our discussion of  $\eta_t$  with the recent measurement performed in Ref. [10], which assumes  $m_t = m_t^{\text{MC}} = 172.5$  GeV and  $M_{\eta_t} = 343$  GeV (and thus implies  $E_{\text{bind}} = -2$  GeV) and reports  $\sigma(pp \rightarrow \eta_t) = 8.8_{-1.4}^{+1.2}$  pb. However, as we discussed in Section 2.1, the properties of toponia are subject to the uncertainties in  $m_t$  and  $\mu_R$ , which have not been taken into account by the experimental search. Furthermore, while Ref. [10] chooses to use a fixed Monte Carlo mass  $m_t^{\text{MC}}$  to perform the study, in contrast to our choice to use the measured pole mass  $m_t^{\text{pole}} = 172.4 \pm 0.7$  GeV [19], this choice should be scrutinized with more care since the value of  $m_t$  will influence the outcome of the kinematic analysis.<sup>2</sup> To see what these might imply, we show the contours derived from varying  $\kappa \equiv \mu_R \times r$  on the  $M_{\eta_t}$ - $\sigma(pp \rightarrow \eta_t)$  plane with  $m_t$  chosen to be 172.4 GeV, 172.4 + 0.7 GeV, and 172.4 - 0.7 GeV in Figure 3, in which we also show the experimental result at 1 $\sigma$  and 95% confidence level (CL). Again, we ignore the  $K$ -factor since it is close to one as discussed in Ref. [9]. One can see that the theoretical contours cover a large area of the  $M_{\eta_t}$ - $\sigma$  plane under the variation of  $m_t$  and  $\kappa$ , signaling that the experimental result should be further improved to properly reflect these uncertainties. Moreover, while the theoretical predictions here are obtained with the MSTW 2008 NNLO PDF [43], it is also important to consider the uncertainties arising from different PDF choices, although we have checked that most will agree within systematic errors. Therefore, it remains an open issue for experimental searches to properly account for the underlying theoretical uncertainties in the  $\eta_t$  measurement to test the SM QCD, which could then later be used to more rigorously probe certain BSM physics, as we will discuss with an explicit example in Section 4.

While  $\eta_t$  has already been discovered at the LHC with a significance of over 5 $\sigma$  in the gluon fusion channel via the individual top decays, it is valid to ask what other avenues we can use to study its properties. One possibility is to probe its next-to-leading annihilation decay to  $ZH$ , which has a branching ratio of roughly  $1.02 \times 10^{-3}$ . Along with the measured production cross section  $\sigma(pp \rightarrow \eta_t) = 8.8$  pb, one obtains  $\sigma(pp \rightarrow \eta_t \rightarrow ZH) = 8.98$  fb at the 13-TeV LHC. Compared to the continuous background with  $\sigma(pp \rightarrow ZH) = 579$  fb, one gets a naively estimated significance of 4.4 $\sigma$  with an integrated luminosity of  $\mathcal{L} = 139$  fb $^{-1}$ . Assuming that the total cross section increases by  $\mathcal{O}(1)$  at the 14-TeV HL-LHC, then, along with the expected  $\mathcal{L} = 3$  ab $^{-1}$ , the naive significance will increase to  $\sim 20\sigma$ . Therefore, if the inclusive final states of all possible  $ZH$  decays can be efficiently reconstructed, this process could possibly be investigated at the HL-LHC. Furthermore, a precise measurement of the branching ratio of  $\eta_t \rightarrow ZH$  could be used to measure the top Yukawa coupling.

Another promising channel is  $gg \rightarrow \eta_t b\bar{b}$ , an example Feynman diagram of which can be found in Figure 4(a). Taking into account only the QCD-induced diagrams and using the projection method, one gets  $\sigma(pp \rightarrow \eta_t b\bar{b}) = 11.0$  pb at the 13-TeV LHC. Compared to the continuous background with  $\sigma(pp \rightarrow t\bar{t}b\bar{b}) = 24.8$  pb, the signal cross section is almost on the same order of magnitude, and thus this process is also likely to be probed both at the current LHC and at the future HL-LHC.

On the other hand,  $\eta_t$  is less likely to be directly produced at lepton colliders due to its  $J^{PC}$  property, which prohibits its singular production through the process  $e^+e^- \rightarrow \eta_t$  given the tiny

<sup>2</sup>For a detailed discussion of different definitions of the top quark mass and how they can be measured from experiments, see Ref. [42].

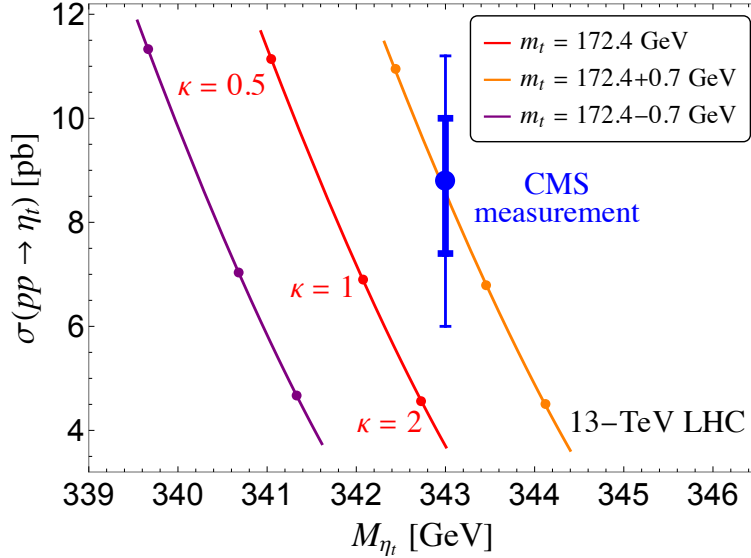


Figure 3: The theoretical contours on the  $M_{\eta_t}$ - $\sigma(pp \rightarrow \eta_t)$  (13-TeV LHC) plane derived from varying  $\kappa \equiv \mu_R \times r$  with  $m_t = 172.4$  GeV (red),  $m_t = 172.4 + 0.7$  GeV (orange), and  $m_t = 172.4 - 0.7$  GeV (purple), respectively, according to the pole mass  $m_t^{\text{pole}} = 172.4 \pm 0.7$  GeV reported in Ref. [19]. We also present the experimental result reported in Ref. [10] at  $1\sigma$  (thick blue line) and 95% CL (thin blue line) assuming  $m_t = m_t^{\text{MC}} = 172.5$  GeV and  $M_{\eta_t} = 343$  GeV. We neglect the  $K$ -factor since it is close to one as discussed in Ref. [9].

electron mass. Some other possible production mechanisms include  $e^+e^- \rightarrow \eta_t \gamma$ ,  $e^+e^- \rightarrow \eta_t Z$ , and  $e^+e^- \rightarrow \eta_t H$  [see Figure 4(b) for an example Feynman diagram of  $e^+e^- \rightarrow \eta_t \gamma$ ]. Since the currently proposed  $\sqrt{s}$  of the future lepton colliders listed in Table 3 are all only slightly above the  $t\bar{t}$  threshold, we only consider the  $e^+e^- \rightarrow \eta_t \gamma$  process. Taking  $\sqrt{s} = 360$  GeV, which is proposed by both CEPC and FCC-ee, one obtains  $\sigma(e^+e^- \rightarrow \eta_t \gamma) = 8.87 \times 10^{-3}$  fb after applying the transverse momentum cut  $p_T^\gamma > 10$  GeV and pseudo-rapidity cut  $|\eta_\gamma| < 3.0$  on the photon. Compared to the continuous background with the same cuts applied, which has  $\sigma(e^+e^- \rightarrow t\bar{t}\gamma) = 8.57$  fb, it is clear that  $\eta_t$  is unlikely to be probed via this process and thus at lepton colliders in general.

### 3.2 $\psi_t$

For the  $\psi_t$  state, since it cannot be produced singularly through gluon fusion as prohibited by the Landau-Yang theorem [29, 30], we consider several associated production mechanisms:  $gg \rightarrow \psi_t g$ ,  $gg \rightarrow \psi_t b\bar{b}$ , and  $q\bar{q}' \rightarrow \psi_t W$  at the LHC and  $e^+e^- \rightarrow \psi_t$  at lepton colliders. For the first process, the parton-level associated production cross section is given by

$$\hat{\sigma}(gg \rightarrow \psi_t g) = \frac{10\pi\alpha_s^3}{9M\hat{s}^2(\hat{s} - M^2)^2(\hat{s} + M^2)^3} |R_S(0)|^2 \left[ (\hat{s}^2 - M^4)(2\hat{s}^3 + M^2\hat{s}^2 + 4M^4\hat{s} + M^6) - 2M^4\hat{s}(M^4 + 2M^2\hat{s} + 5\hat{s}^2) \log\left(\frac{\hat{s}}{M^2}\right) \right], \quad (3.1)$$

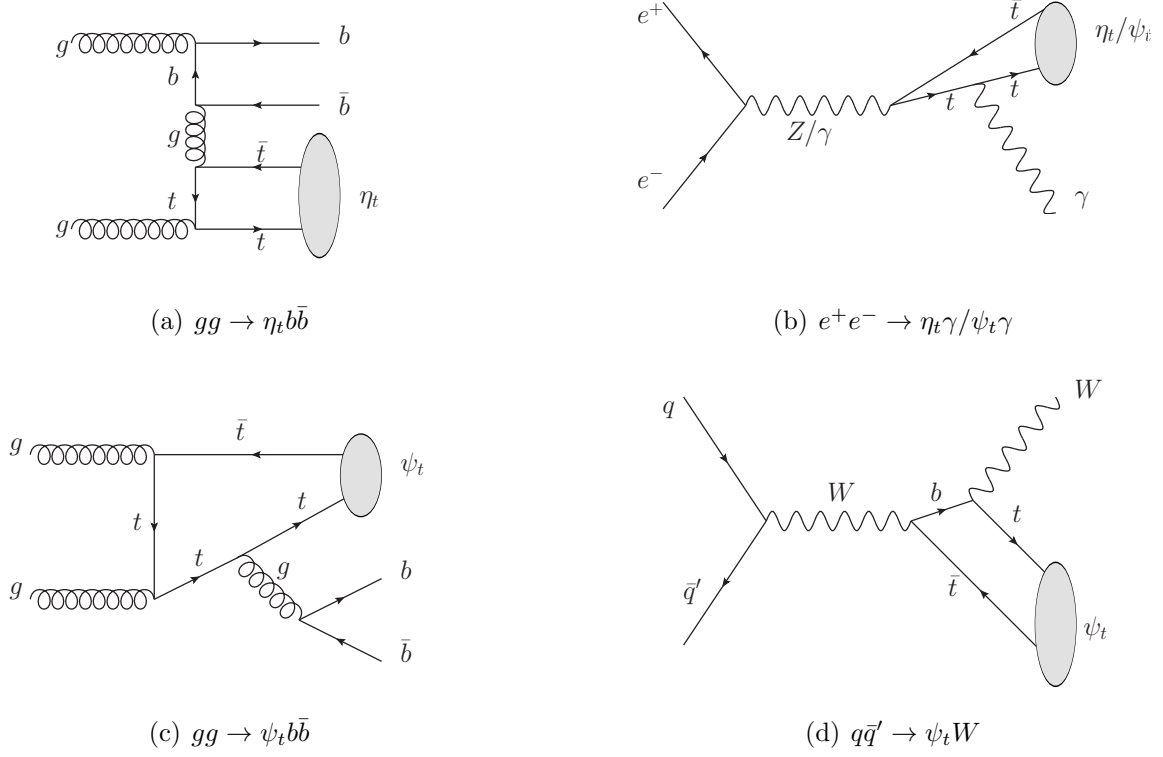


Figure 4: Example Feynman diagrams of the specified processes considered in this study.

which gives the proton-level cross section  $\sigma(pp \rightarrow \psi_t g) = 73.3$  fb at the 13-TeV LHC. Here,  $M = M_{\psi_t}$ . This result is overwhelmed by the continuous production  $\sigma(pp \rightarrow t\bar{t} + j) = \mathcal{O}(10^3)$  pb. For the second process, the cross section given by the QCD-induced diagrams [see for example Figure 4(c)] is  $\sigma(pp \rightarrow \psi_t b\bar{b}) \sim \mathcal{O}(2)$  fb at the 13-TeV LHC, while the electroweak contribution is  $\sim \mathcal{O}(0.3)$  fb, the combined result of which is significantly prevailed by both the continuous background with  $\sigma(pp \rightarrow t\bar{t}b\bar{b}) = 24.8$  pb and the  $\eta_t$ -induced background with  $\sigma(pp \rightarrow \eta_t b\bar{b}) = 11.0$  pb. Finally, for the third process [see for example Figure 4(d)], the associated cross section is  $\sigma(pp \rightarrow \psi_t W) = 0.09$  fb at the 13-TeV LHC, which is again overwhelmed by the continuous background with  $\sigma(pp \rightarrow t\bar{t}W) = 369$  fb. Therefore, we conclude that it is unlikely to probe  $\psi_t$  at both the current LHC and the future HL-LHC.

On the other hand, the production of  $\psi_t$  at lepton colliders has been widely studied in the literature (see for example Refs. [23, 26–28]). In particular, both CEPC [31] and FCC-ee [34, 35] propose to run at the  $t\bar{t}$  threshold around  $\sqrt{s} \sim 360$  GeV, which would most likely further cover the mass pole of  $\psi_t$  (together with other excited states) around  $2m_t$ , and thus we briefly discuss the prospect of  $\psi_t$  measurements at future lepton colliders. First of all, we calculate the production cross section  $\sigma(e^+e^- \rightarrow \psi_t)$  around  $\sqrt{s} = M_{\psi_t}$  using both the Green function method and the B-W formula in Figure 5, based on which we further estimate the significance of  $\psi_t$  discovery through its intrinsic decay to  $W^+W^-b\bar{b}$  using the B-W formula. The continuous background  $e^+e^- \rightarrow W^+W^-b\bar{b}$  has a cross section of 30.5 fb at  $\sqrt{s} = M_{\psi_t}$  and increases rapidly after  $\sqrt{s}$  passes through  $2m_t$ . Assuming the reconstruction efficiency of the  $t\bar{t}$  final state to be 27.6% [44], the integrated luminosity to be  $1 \text{ ab}^{-1}$ , and using both the

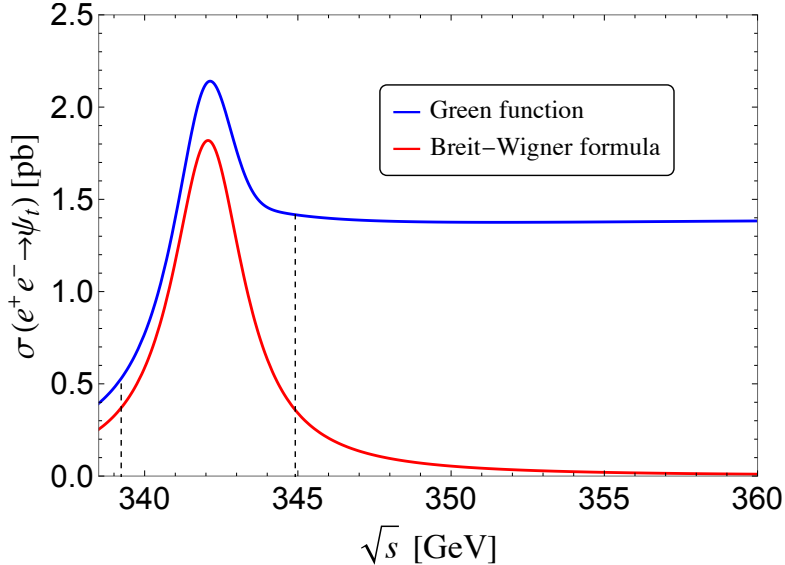


Figure 5: The cross section  $\sigma(e^+e^- \rightarrow t\bar{t})$  as a function of  $\sqrt{s}$  calculated using both the Green function method (blue) and the B-W formula (red). The two dashed lines represent  $m_{t\bar{t}} = M_{\psi_t} \pm \Gamma$ , respectively, between which we identify the “resonance” region, as in Figure 2.

dileptonic and semi-leptonic final states from top decays, one could obtain a significance of more than  $700\sigma$  at  $\sqrt{s} = M_{\psi_t}$  and even  $8\sigma$  at  $\sqrt{s} = 360$  GeV off-resonance. Moreover, in the recent Ref. [12], it is claimed that  $\psi_t$  could be discovered with a significance of over  $5\sigma$  at the CEPC by measuring the cross section ratio  $R_b \equiv \sigma(e^+e^- \rightarrow b\bar{b}) / \sum_{q=u,d,s,c,b} \sigma(e^+e^- \rightarrow q\bar{q})$ . The main idea is to capture the interference effect caused by the  $\psi_t$ -mediated diagrams when  $\sqrt{s}$  passes from below  $M_{\psi_t}$  to above  $M_{\psi_t}$ . As a result of this interference,  $R_b(\sqrt{s})$ , which would only be a flat line around  $\sqrt{s} = M_{\psi_t}$  if only the  $\gamma$ - and  $Z$ -poles were present, will manifest an interference pattern that can facilitate the measurement of the  $\psi_t$ -pole. One major factor that enables this possibility is the relatively large annihilation decay width of  $\psi_t \rightarrow b\bar{b}$  (see Table 2), owing to the  $W$ -mediated contributions that are highly suppressed for down-type quarks of the other generations. Given the even higher branching ratio of the  $\psi_t \rightarrow WW$  decay, it might also be possible to discover  $\psi_t$  in the  $WW$  final state using a similar measurement based on the  $\psi_t$ -pole interference pattern, which we leave to future exploration. Finally, one can also consider the subleading  $\psi_t \rightarrow \gamma H$  decay, which has an overall cross section of  $\sigma(e^+e^- \rightarrow \psi_t \rightarrow \gamma H) = 0.089$  fb at  $\sqrt{s} = M_{\psi_t}$  after applying the cuts  $p_T^\gamma > 10$  GeV and  $|\eta_\gamma| < 3$ . Compared to the continuous background with  $\sigma(e^+e^- \rightarrow \gamma H) = 0.050$  fb after applying the same cuts, it is clear that the signal has a larger cross section, although there could be additional pollutions from other reducible backgrounds. For example, the cross section of the continuous process  $e^+e^- \rightarrow \gamma b\bar{b}$  with the same photon cuts and the additional invariant mass cut  $|m_{b\bar{b}} - m_H| < 2$  GeV applied is 2.35 fb. Without further selection cuts (for instance, the angular distributions of  $b$  and  $\bar{b}$ ), this will lead to a significance of  $1.8\sigma$  assuming  $\mathcal{L} = 1$  ab $^{-1}$ , and thus, similar to the case of  $gg \rightarrow \eta_t \rightarrow ZH$ , the possible measurement of this channel relies on the capability of future experiments to inclusively reconstruct the  $\gamma H$  final state, which, if performed efficiently, will provide another way to discover  $\psi_t$  and even to probe the top Yukawa coupling.

### 3.3 $\chi_t$

For the  $P$ -wave  $\chi_t$  states, we consider both  $\chi_{t0}$  and  $\chi_{t1}$ . Since they are both  $P$ -wave states, their production cross sections are both suppressed by  $|R'_P(0)|^2 \propto \alpha_s^5$ . For  $\chi_{t0}$ , we first consider its production via gluon fusion, whose parton-level cross section is given by

$$\hat{\sigma}(gg \rightarrow \chi_{t0}) = \frac{12\pi^2 \alpha_s^2}{M^3 \hat{s}} |R'_P(0)|^2 \delta(\hat{s} - M^2), \quad (3.2)$$

with  $M = M_{\chi_{t0}}$ , which leads to the proton-level cross section  $\sigma(pp \rightarrow \chi_{t0}) = 10.0$  fb at the 13-TeV LHC. This result is clearly prevailed by both  $\sigma(gg \rightarrow \eta_t) = 8.8$  pb and the continuous  $\sigma(gg \rightarrow t\bar{t}) = 833.9$  pb [10]. On the other hand,  $\sigma(f\bar{f} \rightarrow \chi_{t0}) \propto m_f^2$  is further suppressed by the small fermion masses both at the LHC ( $f$  being the light quarks) and the lepton colliders ( $f$  being the light charged leptons). Therefore, it is unlikely for  $\chi_{t0}$  to be probed at the LHC and other future colliders.

For  $\chi_{t1}$ , again, it cannot be produced via gluon fusion due to the Landau-Yang theorem, but since its coupling to a light fermion pair is not suppressed by the fermion mass, one can consider its production at lepton colliders. One starts from the partial width

$$\Gamma(\chi_{t1} \rightarrow f\bar{f}) = C_f \frac{96 \alpha_{\text{EM}}^2 a_t^2}{(M^2 - m_Z^2)^2 c_w^4 s_w^4} \sqrt{1 - \frac{4m_f^2}{M^2}} \left[ v_f^2 \left( 1 + \frac{2m_f^2}{M^2} \right) + a_f^2 \left( 1 - \frac{4m_f^2}{M^2} \right) \right] |R'_P(0)|^2, \quad (3.3)$$

where  $M = M_{\chi_{t1}}$ ,  $C_f = 1, 3$  is the color factor for leptons and quarks, respectively,  $\alpha_{\text{EM}}$  is the electric fine structure constant,  $c_w \equiv \cos \theta_w$  and  $s_w \equiv \sin \theta_w$  with  $\theta_w$  being the weak angle, and

$$v_i = \frac{I_{3L,i}}{2} - Q_i s_w^2, \quad a_i = \frac{I_{3L,i}}{2}, \quad (3.4)$$

with  $Q_i$  being the electric charge of the fermion  $i$  and  $I_{3L} = +1/2$  ( $-1/2$ ) for up-type quarks and neutrinos (down-type quarks and charged leptons). For  $f = e^-$ , one can use the B-W formula to obtain  $\sigma(e^+e^- \rightarrow \chi_{t1}) = 0.54$  fb. Naively estimating with the cross section of the continuous plus  $\psi_t$  background  $\sigma(e^+e^- \rightarrow t\bar{t}/\psi_t) \approx 1.5$  pb (see Figure 5) at  $\sqrt{s} = M_{\chi_{t1}}$ , one gets a significance of only  $\sim 0.56\sigma$  with even  $\mathcal{L} = 1$  ab $^{-1}$ . Compared to the  $S$ -wave  $\psi_t$  whose differential cross section  $d\sigma/d\theta$  is uniformly distributed across the production angle  $\theta$  of the constituent  $t$  after the decay, that of the  $P$ -wave  $\chi_{t1}$  depends non-trivially on  $\theta$ , and thus one could try to refine the analysis by analyzing the final-state kinematic distributions. However, we do not expect the significance to improve up to  $5\sigma$  even after performing such analysis. On the other hand,  $\sigma(q\bar{q} \rightarrow \chi_{t1})$  at the LHC still suffers from the large continuous  $t\bar{t}$  background as in the case of  $\chi_{t0}$ . Therefore, we conclude that it is also unlikely to probe  $\chi_{t1}$  at the LHC and other future colliders.

## 4 Toponium as a probe for the real singlet extension

In addition to probing the toponium states themselves, we further consider the prospect of probing BSM physics using the toponium measurement. Here we use the real singlet extension to the SM (SSM) as an example, though one can certainly generalize the framework to other

BSM models. For simplicity, we consider the  $\mathbb{Z}_2$ -symmetric SSM, in which one introduces a  $\mathbb{Z}_2$ -odd real scalar  $S$ . Along with the SM Higgs doublet  $\Phi$ , the most general renormalizable scalar potential of the SSM is given by

$$V(\Phi, S) = -\mu^2 \Phi^\dagger \Phi - m^2 S^2 + \lambda_1 (\Phi^\dagger \Phi)^2 + \lambda_2 S^4 + \lambda_3 S^2 \Phi^\dagger \Phi, \quad (4.1)$$

where we follow the coupling normalization convention of Ref. [45]. Parameterizing the fields as  $\Phi = (0, \frac{h_1+v}{\sqrt{2}})^T$  and  $S = \frac{h_2+x}{\sqrt{2}}$ , where  $v$  and  $x$  denote the vacuum expectation values (VEVs) of the fields, respectively, one obtains the minimization conditions

$$m^2 = \lambda_1 v^2 + \frac{\lambda_3}{2} x^2, \quad \mu^2 = \lambda_2 x^2 + \frac{\lambda_3}{2} v^2, \quad (4.2)$$

which lead to the mass matrix in the  $(h_1, h_2)^T$  basis as

$$M^2 = \begin{pmatrix} 2\lambda_1 v^2 & \lambda_3 v x \\ \lambda_3 v x & 2\lambda_2 x^2 \end{pmatrix}. \quad (4.3)$$

Denoting  $\alpha$  as the mixing angle between  $h_{1,2}$ , one gets the mixing matrix

$$\begin{pmatrix} \phi \\ H \end{pmatrix} = \begin{pmatrix} \cos \alpha & \sin \alpha \\ -\sin \alpha & \cos \alpha \end{pmatrix} \begin{pmatrix} h_1 \\ h_2 \end{pmatrix}, \quad (4.4)$$

where we identify  $H$  with the 125-GeV Higgs boson observed at the LHC and  $\phi$  with the exotic mass eigenstate with  $m_\phi < m_H = 125$  GeV. Under this mixing convention, the SM Higgs is recovered at the decoupling limit  $\sin \alpha = -1$ . Consequently, one can write down the top Yukawa interaction in the mass basis as

$$\mathcal{L}_{\text{Yuk}} = -\frac{m_t}{v} (\phi \cos \alpha - H \sin \alpha) \bar{t} t, \quad (4.5)$$

which, in the position space, leads to the Yukawa potential

$$V_{\text{Yuk}}(r) = -\frac{1}{4\pi r} \left[ \left( \frac{m_t \cos \alpha}{v} \right)^2 e^{-m_\phi r} + \left( \frac{m_t \sin \alpha}{v} \right)^2 e^{-m_H r} \right]. \quad (4.6)$$

As a result, the static potential given in Eq. (2.6) will be modified by the inclusion of the  $\phi$ - and  $H$ -mediated Yukawa potentials, which allows us to use the  $\eta_t$  production measurement performed in Ref. [10] to indirectly infer the existence of additional scalar fields coupling to the top quark. Here, the Yukawa potential mediated by the 125-GeV Higgs boson is suppressed by a factor of  $e^{-m_H a_t} \sim \mathcal{O}(10^{-3})$  and thus will not influence the properties of toponium, as already pointed out in Ref. [4]. On the contrary, the light scalar  $\phi$  field could constructively contribute to the static potential (for a color-singlet toponium) and enhance the effective couplings within the toponium system with great significance.

On the other hand, the current Higgs exotic decay can also be used to constrain this model. Denoting  $\tan \beta \equiv v/x$ , the width of the decay channel  $H \rightarrow \phi\phi$  for  $m_\phi < m_H/2$  is given by [45]

$$\Gamma(H \rightarrow \phi\phi) = \frac{1}{8\pi m_H} \sqrt{1 - \frac{4m_\phi^2}{m_H^2}} \left[ \frac{\sin 2\alpha}{2v} (\tan \beta \sin \alpha + \cos \alpha) \left( m_\phi^2 + \frac{m_H^2}{2} \right) \right]^2. \quad (4.7)$$

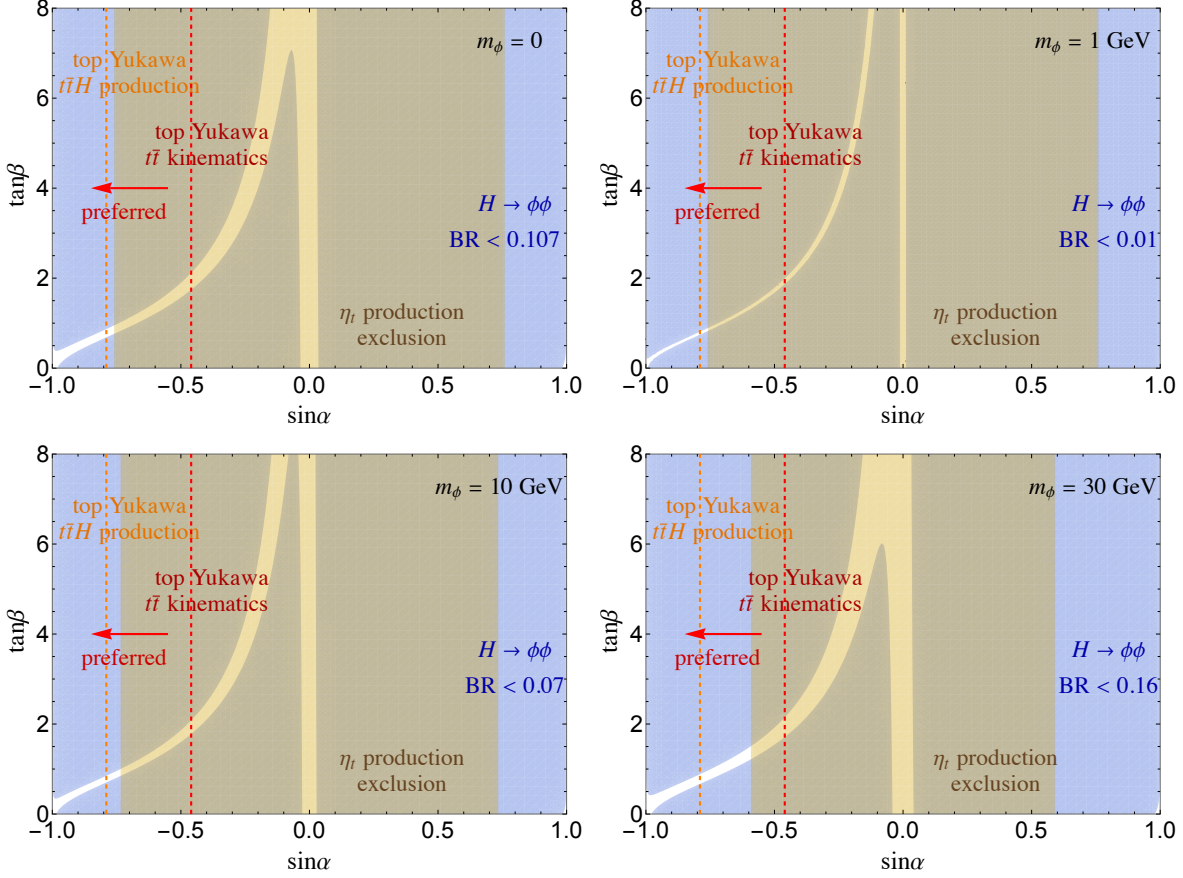


Figure 6: The 95% CL constraint on  $\text{BR}(H \rightarrow \phi\phi)$  obtained from Refs. [19, 46] (blue) and that imposed by the  $\eta_t$  production measurement performed in Ref. [10] (brown) on the  $(\sin \alpha)$ – $(\tan \beta)$  plane for four benchmark masses  $m_\phi = 0, 1, 10, 30$  GeV. We also show the preferred regions (red arrow) by the 125-GeV Higgs top Yukawa coupling measurements at 95% CL summarized in Ref. [42] with two dashed lines: the red one is measured through the  $t\bar{t}$  kinematics [47] and the orange one through the  $t\bar{t}H$  production cross section [48, 49].

We show the 95% CL constraint on  $\text{BR}(H \rightarrow \phi\phi)$  on the  $(\sin \alpha)$ – $(\tan \beta)$  plane obtained from Ref. [19, 46] for four benchmark masses  $m_\phi = 0, 1, 10, 30$  GeV in Figure 6. The 95% CL constraints with regard to the Yukawa potential variation derived from the  $\eta_t$  measurement are also presented in Figure 6, from which one can see that for all four benchmark masses, the allowed parameter space by the  $\text{BR}(H \rightarrow \phi\phi)$  constraint, which roughly follows the  $\tan \beta \sin \alpha + \cos \alpha = 0$  contour that gives  $\text{BR}(H \rightarrow \phi\phi) = 0$ , is further ruled out by the  $\eta_t$  production measurement down to the region around  $(\sin \alpha, \tan \beta) = (-1, 0)$ . Since the top Yukawa coupling of the 125-GeV Higgs boson is also modified, as shown in Eq. (4.5), we show in Figure 6 the preferred ranges of  $\sin \alpha$  by two types of top Yukawa coupling measurements (see Ref. [42] for a review): the direct measurement of  $t\bar{t}H$  production cross section gives  $y_t = 0.95^{+0.07}_{-0.08}$  [48, 49], while the measurement of the loop-induced correction to the kinematic distribution of the  $t\bar{t}$  final state, which mainly comes from the top Yukawa coupling between  $t$  and  $\bar{t}$ , gives  $y_t = 1.16^{+0.24}_{-0.35}$  [47]. It can be seen that the exclusion by the  $\eta_t$  measurement has not yet reached the current limits imposed by the top Yukawa coupling measurements. However, as future measurements of  $\eta_t$

are expected to improve further, they could potentially exclude a larger region of the parameter space. Finally, while we only present the study on the SSM as an example, one can certainly generalize this framework to other BSM models that afford a more sophisticated top Yukawa coupling structure, for which the  $\eta_t$  measurement may impose a more non-trivial constraint.

## 5 Discussion and conclusions

We remark again that, as we have discussed and demonstrated in Section 3.1 through Figure 3, the theoretical prediction of toponium properties performed in Ref. [10] still suffers from the uncertainty arising from various sources such as the top quark mass, renormalization scale, and parton distribution function. Therefore, it is important to revisit the analysis to pin down the production cross section  $\sigma(pp \rightarrow \eta_t)$  in a more rigorous manner, which, along with the measured toponium mass, could provide a measure for the top quark mass and width (see Ref. [42] for a review of the existing top quark mass measurements). Since  $\eta_t$  and  $\psi_t$  have approximately the same mass, a precise measurement of the  $\eta_t$  mass at the HL-LHC can help determine the center-of-mass energy around the  $t\bar{t}$  threshold to be scanned at both the CEPC and FCC-ee (see Ref. [50] for the N<sup>3</sup>LO QCD calculation and Ref. [51] for projected measurements of the top quark mass and width near the  $t\bar{t}$  threshold region at a future lepton collider).

Besides the projection and Green function methods, one can also use the ‘‘bound state effective field theory (BSEFT)’’ to study toponium decays and production, such as introduced in Ref. [38]. However, since the effective couplings in the BSEFT are derived under the assumption that all participant particles are on-shell, it can only be used to study the processes in which the fields interacting with the toponium are all external. For example, the  $\psi_t b\bar{b}$  vertex derived from the BSEFT is given by  $\bar{b}\gamma_\mu(g_{\psi_t}^V - g_{\psi_t}^A\gamma^5)b\psi_t^\mu$ , where

$$g_{\psi_t}^V = -\sqrt{\frac{(C_F\alpha_s)^3\pi}{3}}\frac{\alpha_{\text{EM}}}{12}\left\{\frac{m_t^2}{s_w^2}\left[\frac{4(8c_w^2+1)s_w^2-9}{c_w^2(Q^2-m_Z^2)}+\frac{3(2-K^2/m_W^2)}{K^2-m_W^2}\right]-8\frac{4m_t^2}{Q^2}\right\}, \quad (5.1)$$

$$g_{\psi_t}^A = \sqrt{\frac{(C_F\alpha_s)^3\pi}{3}}\frac{\alpha_{\text{EM}}m_t^2}{4s_w^2}\left[\frac{3-8s_w^2}{c_w^2(Q^2-m_Z^2)}-\frac{2-K^2/m_W^2}{K^2-m_W^2}\right], \quad (5.2)$$

with  $k_{1,2}$  denoting the outgoing momenta of  $b$  and  $\bar{b}$ , respectively, and, for simplicity,  $Q^2 \equiv (k_1+k_2)^2 = M_{\psi_t}^2$  and  $K^2 \equiv (k_1-k_2)^2/4 = -M_{\psi_t}^2/4$  in the  $m_b \rightarrow 0$  limit. However, in the general case where  $b$  and  $\bar{b}$  are not necessarily on-shell, not only will  $Q^2$  and  $K^2$  depend on the exact kinematics of the scattering process, but there will also be an additional term  $\propto K^\mu$  that can only be captured by the projection method. We have checked that this discrepancy will lead to a huge difference in the predicted production cross section of the  $pp \rightarrow \psi_t b\bar{b}$  process, which is also the case for other interactions and corresponding production mechanisms. Therefore, one should be careful about using the BSEFT to study toponium phenomenology.

In addition to the physics discussed in the main text, one might also consider probing CP-violation in the top Yukawa coupling via the annihilation decay modes of toponia that involve  $H$ . For instance, in the presence of CP-violation, the  $\psi_t \rightarrow \gamma H$  decay width [see Eq. (A.13) for the corresponding formula] will scale from  $|y_t^2| \rightarrow |y_t|^2 + |y_t'|^2$ ,  $y_t$  and  $y_t'$  denoting the possible CP-even and CP-odd components of top Yukawa coupling, respectively, while some originally forbidden decay modes such as  $\eta_t \rightarrow HH$  will be turned on. Similar analysis can be performed

with the search for  $\eta_t \rightarrow ZH$ . Although these effects are tightly constrained by the experimental measurements to date, it still remains an interesting question whether one can use these toponium decays to probe certain BSM physics that introduces CP-violation.

In conclusion, we have calculated some theoretical properties of toponia, including their masses, decays, and production at colliders. To study their annihilation decay modes and production mechanisms, we have adopted both projection and Green function methods and found that they both gave comparable results to the CMS measurement of the  $pp \rightarrow \eta_t$  production cross section at the 13-TeV LHC. Using the projection method, we have studied the sensitivity of the four lowest-lying toponium states at the current LHC and future HL-LHC, CEPC, and FCC-ee, where we have found that  $\eta_t$  is likely to be probed via various other channels at the hadron colliders and  $\psi_t$  at the lepton colliders, while the other two  $P$ -wave states,  $\chi_{t0}$  and  $\chi_{t1}$ , seem unlikely to be probed in the near future. Finally, we have also used the SSM as an example to show how one can constrain the parameter space of BSM models with the  $\eta_t$  measurement.

## Acknowledgments

We thank Kaoru Hagiwara for useful discussions. This work is supported by the U.S. Department of Energy under the contract DE-SC-0017647 and DEAC02-06CH11357 at Argonne National Laboratory. TKC is also supported by the Ministry of Education, Taiwan, under the Government Scholarship to Study Abroad.

## A Partial width formulas for the annihilation decay modes

In this appendix, we summarize the formulas for the annihilation decay widths of the toponium states adapted from Refs. [2, 3, 22]. We denote  $x_X \equiv m_X^2/M^2$ , where  $M$  is the mass of the corresponding toponium, and define the Källén function  $\lambda(a, b, c) \equiv \sqrt{a^2 + b^2 + c^2 - 2ab - 2bc - 2ca}$ . For  $\psi_t \rightarrow b\bar{b}$  and  $\chi_{t1} \rightarrow b\bar{b}$ , there is an additional contribution from the  $W$ -exchange diagrams compared to the other  $f\bar{f}$  decay modes. To turn on this specifically for  $f = b$ , we define  $\delta_{fb} = 1$  if  $f = b$  and  $\delta_{fb} = 0$  if otherwise. For simplicity, we set  $m_f = 0$  in the following expressions.

- $\eta_t$  ( $0^{-+}$ ):

$$\Gamma(\eta_t \rightarrow W^+W^-) = \frac{3\alpha_{\text{EM}}^2}{2M^2s_w^4(1-4x_W)^2} \lambda^{3/2}(1, x_W, x_W) |R_S(0)|^2, \quad (\text{A.1})$$

$$\Gamma(\eta_t \rightarrow ZZ) = \frac{\alpha_{\text{EM}}^2(32s_w^4 - 24s_w^2 + 9)^2}{432M^2s_w^4c_w^4(1-2x_Z)^2} \lambda^{3/2}(1, x_Z, x_Z) |R_S(0)|^2, \quad (\text{A.2})$$

$$\Gamma(\eta_t \rightarrow ZH) = \frac{3\alpha_{\text{EM}}^2}{64M^2s_w^4c_w^4x_Z^2} \lambda^{3/2}(1, x_H, x_Z) |R_S(0)|^2, \quad (\text{A.3})$$

$$\Gamma(\eta_t \rightarrow \gamma\gamma) = \frac{64\alpha_{\text{EM}}^2}{27M^2} |R_S(0)|^2, \quad (\text{A.4})$$

$$\Gamma(\eta_t \rightarrow \gamma Z) = \frac{2\alpha_{\text{EM}}^2(3-8s_w^2)^2}{27M^2s_w^2c_w^2} \lambda^{1/2}(1, 0, x_Z) |R_S(0)|^2, \quad (\text{A.5})$$

$$\Gamma(\eta_t \rightarrow gg) = \frac{8\alpha_s^2}{3M^2} |R_S(0)|^2 . \quad (\text{A.6})$$

•  $\psi_t (1^{--})$ :

$$\Gamma(\psi_t \rightarrow f\bar{f}) = \frac{4C_f\alpha_{\text{EM}}^2}{M^2} \left\{ \left[ \frac{2}{3}Q_f + \frac{v_f(1 - \frac{8}{3}s_w^2)}{4s_w^2c_w^2(1-x_Z)} - \frac{\delta_{fb}(1+8x_W)}{48s_w^2(1+4x_W)x_W} \right]^2 + \left[ \frac{a_f(1 - \frac{8}{3}s_w^2)}{4s_w^2c_w^2(1-x_Z)} - \frac{\delta_{fb}(8x_W+1)}{48s_w^2(1+4x_W)x_W} \right]^2 \right\} |R_S(0)|^2 , \quad (\text{A.7})$$

$$\Gamma(\psi_t \rightarrow W^+W^-) = \frac{\alpha_{\text{EM}}^2}{64M^2x_W^2s_w^4} \lambda^{3/2}(1, x_W, x_W) \left[ \frac{1+20x_W+12x_W^2}{(1-x_Z)^2} \left( 1 - \frac{16}{3}s_w^2x_Z + \frac{64}{9}s_w^4x_Z^2 \right) - \frac{8x_W(5+6x_W)(1-\frac{8}{3}s_w^2x_Z)}{(1-4x_W)(1-x_Z)} + \frac{16x_W(2-x_W)}{(1-4x_W)^2} \right] |R_S(0)|^2 , \quad (\text{A.8})$$

$$\Gamma(\psi_t \rightarrow ZZ) = \frac{\alpha_{\text{EM}}^2(1 - \frac{8}{3}s_w^2)^2}{32M^2s_w^4c_w^4(1-2x_Z)^2x_Z} \lambda^{5/2}(1, x_Z, x_Z) |R_S(0)|^2 , \quad (\text{A.9})$$

$$\Gamma(\psi_t \rightarrow \gamma H) = \frac{4\alpha_{\text{EM}}y_t^2}{9\pi M^2}(1-x_H) |R_S(0)|^2 = \frac{2\alpha_{\text{EM}}}{9\pi v_{\text{EW}}^2}(1-x_H) |R_S(0)|^2 , \quad (\text{A.10})$$

$$\Gamma(\psi_t \rightarrow ZH) = \frac{\alpha_{\text{EM}}^2(1 - \frac{8}{3}s_w^2)^2}{32M^2s_w^4c_w^4} \lambda^{1/2}(1, x_H, x_Z) \times \frac{[(1-x_Z)^2 - x_H(1-3x_Z)]^2 + \frac{1}{2}x_Z[(1-x_Z)^2 + x_H(2-x_H)]^2}{x_Z(1-x_Z)^2(1-x_Z-x_H)^2} |R_S(0)|^2 , \quad (\text{A.11})$$

$$\Gamma(\psi_t \rightarrow \gamma Z) = \frac{2\alpha_{\text{EM}}^2(1-x_Z^2)}{9M^2s_w^2c_w^2x_Z} |R_S(0)|^2 , \quad (\text{A.12})$$

$$\Gamma(\psi_t \rightarrow 3g) = \frac{40(\pi^2-9)\alpha_s^3}{81\pi M^2} |R_S(0)|^2 . \quad (\text{A.13})$$

•  $\chi_{t0} (0^{++})$ :

$$\Gamma(\chi_{t0} \rightarrow W^+W^-) = \frac{3\alpha_{\text{EM}}^2}{4M^4s_w^4x_W^2} \lambda^{1/2}(1, x_W, x_W) \left\{ \left[ \frac{2(1-x_W)}{1-4x_W} - \frac{3(1-2x_W)}{2(1-x_H)} \right]^2 + 2x_W^2 \left[ \frac{2}{1-4x_W} + \frac{3}{1-x_H} \right]^2 \right\} |R'_P(0)|^2 , \quad (\text{A.14})$$

$$\Gamma(\chi_{t0} \rightarrow ZZ) = \frac{96\alpha_{\text{EM}}^2}{M^4s_w^4c_w^4x_Z^2} \lambda^{1/2}(1, x_Z, x_Z) \left\{ \left[ \frac{(1-\frac{8}{3}s_w^2)^2x_Z^2}{8(1-2x_Z)^2} - \frac{1}{16} + \frac{3}{32} \frac{1-2x_Z}{1-x_H} \right]^2 + \frac{1}{2}x_Z^2 \left[ \frac{-(1-\frac{8}{3}s_w^2)^2(3-8x_Z) + (3-4x_Z)}{16(1-2x_Z)} - \frac{3}{8(1-x_H)} \right]^2 \right\} |R'_P(0)|^2 , \quad (\text{A.15})$$

$$\Gamma(\chi_{t0} \rightarrow HH) = \frac{3\alpha_{\text{EM}}^2}{32M^4s_w^4x_W^2}\lambda^{1/2}(1, x_H, x_H) \left[ \frac{5-8x_H}{(1-2x_H)^2} - \frac{9x_H}{1-x_H} \right]^2 |R'_P(0)|^2, \quad (\text{A.16})$$

$$\Gamma(\chi_{t0} \rightarrow \gamma\gamma) = \frac{256\alpha_{\text{EM}}^2}{3M^4} |R'_P(0)|^2, \quad (\text{A.17})$$

$$\Gamma(\chi_{t0} \rightarrow Z\gamma) = \frac{24\alpha_{\text{EM}}^2}{M^4s_w^2c_w^2} \left(1 - \frac{8}{3}s_w^2\right)^2 \frac{(1 - \frac{1}{3}x_Z)^2}{1-x_Z} |R'_P(0)|^2, \quad (\text{A.18})$$

$$\Gamma(\chi_{t0} \rightarrow gg) = \frac{96\alpha_s^2}{M^4} |R'_P(0)|^2. \quad (\text{A.19})$$

•  $\chi_{t1} (1^{++})$ :

$$\Gamma(\chi_{t1} \rightarrow f\bar{f}) = \frac{96C_f\alpha_{\text{EM}}^2}{M^4} \left\{ \left[ \frac{a_f}{4s_w^2c_w^2(1-x_Z)} - \frac{\delta_{fb}(-1+8x_W)}{48s_w^2(1+4x_W)x_W} \right]^2 + \left[ \frac{v_f}{4s_w^2c_w^2(1-x_Z)} - \frac{\delta_{fb}(-1+8x_W)}{48s_w^2(1+4x_W)x_W} \right]^2 \right\} |R'_P(0)|^2, \quad (\text{A.20})$$

$$\Gamma(\chi_{t1} \rightarrow W^+W^-) = \frac{3\alpha_{\text{EM}}^2}{2M^4s_w^4x_W(1-4x_W)^2}\lambda^{3/2}(1, x_W, x_W) \left[ \frac{64x_W^2}{1-4x_W} + 4 \left( \frac{x_Z-4x_W}{1-x_Z} \right)^2 + \frac{(1+4x_W-2x_Z)^2(1+4x_W+12x_W^2)}{4x_W(1-x_Z)^2} \right] |R'_P(0)|^2, \quad (\text{A.21})$$

$$\Gamma(\chi_{t1} \rightarrow ZZ) = \frac{3\alpha_{\text{EM}}^2}{16M^4s_w^4c_w^4x_Z(1-2x_Z)^2}\lambda^{5/2}(1, x_Z, x_Z) \left[ 1 - \frac{2(1 - \frac{8}{3}s_w^2)^2x_Z}{1-2x_Z} \right]^2 |R'_P(0)|^2, \quad (\text{A.22})$$

$$\Gamma(\chi_{t1} \rightarrow ZH) = \frac{3\alpha_{\text{EM}}^2}{8s_w^4c_w^4M^4x_Z^2(1-x_Z-x_H)^2}\lambda^{1/2}(1, x_Z, x_H) \times \left\{ (1+x_Z-x_H)^2 \left( 1-x_Z + \frac{x_Hx_Z}{1-x_Z} \right)^2 + \frac{1}{2}x_Z \right. \\ \left. \times \left[ 3-3x_Z+x_H+4x_Hx_Z \left( \frac{1}{1-x_Z} + \frac{1}{1-x_Z-x_H} \right) \right]^2 \right\} |R'_P(0)|^2, \quad (\text{A.23})$$

$$\Gamma(\chi_{t1} \rightarrow \gamma Z) = \frac{16\alpha_{\text{EM}}^2}{3M^4s_w^2c_w^2} \left(1 - \frac{8}{3}s_w^2\right)^2 \frac{x_Z(1+x_Z)}{1-x_Z} |R'_P(0)|^2. \quad (\text{A.24})$$

## B Green function method for $P$ -wave states

In this appendix, we compare the Green function and projection methods for  $P$ -wave toponium states. Following Ref. [52], one can write down

$$\sigma(gg \rightarrow t\bar{t} \rightarrow bW^+\bar{b}W^-)_P = \sigma(gg \rightarrow t\bar{t} \rightarrow bW^+\bar{b}W^-)_{P,\text{tree}} \frac{\text{Im}[\nabla^2 G(r, E)]_{r=0}}{\text{Im}[\nabla^2 G_0(r, E)]_{r=0}}, \quad (\text{B.1})$$

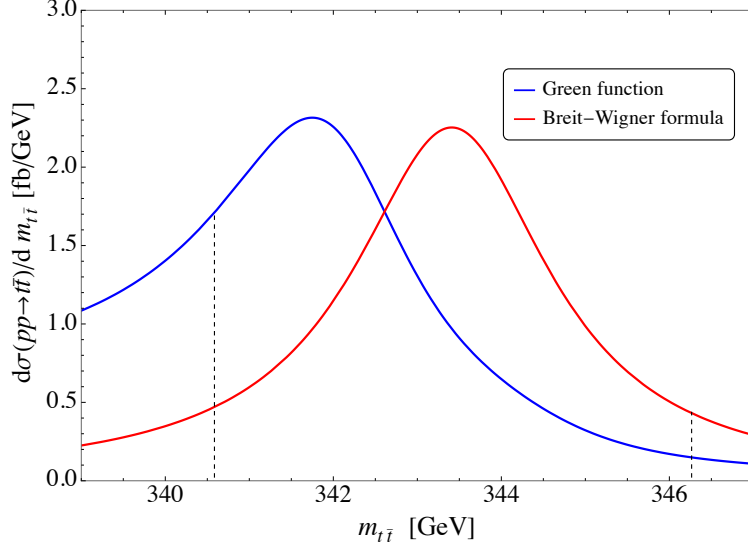


Figure 7: The  $d\sigma(pp \rightarrow \chi_{t0})/dm_{t\bar{t}}$  distributions at the 13-TeV LHC calculated from the leading-order Green function method and B-W formula. The two dashed lines represent  $m_{t\bar{t}} = M_{\chi_{t0}} \pm \Gamma$  with  $M_{\chi_{t0}} = 343.43$  GeV and  $\Gamma = 2.84$  GeV, respectively, between which we identify the  $t\bar{t}$  system to be on “resonance”.

where, approximating the static potential with  $V_{\text{Coul}}$  and using Eq. (2.21), one has

$$\mathcal{S}_P(E) \equiv \frac{\text{Im}[\nabla^2 G(r, E)]_{r=0}}{\text{Im}[\nabla^2 G_0(r, E)]_{r=0}} = \frac{\text{Im} \left[ -a^2 \log(-2i\sqrt{z'}) - a^2 \psi^{(0)} \left( 1 - i\frac{a}{2\sqrt{z'}} \right) + ia\sqrt{z'} + z' \right]}{\text{Im}[z']}. \quad (\text{B.2})$$

Using the  $\chi_{t0}$  state for example, its parton-level production cross section  $\hat{\sigma}(gg \rightarrow t\bar{t})_{3P_0, \text{tree}}$  near the threshold is given by

$$\hat{\sigma}(gg \rightarrow t\bar{t})_{3P_0, \text{tree}} = \frac{\pi \alpha_s^2 (24m_t^2 + \hat{s})}{144 \hat{s} (2m_t + \sqrt{\hat{s}})^2} \left( 1 - \frac{4m_t^2}{\hat{s}} \right)^{\frac{3}{2}}, \quad (\text{B.3})$$

where we have simply assumed  $M = 2m_t$ . We show the corresponding proton-level differential cross section  $d\sigma(pp \rightarrow t\bar{t})/dm_{t\bar{t}}$  derived from the Green function as well as the B-W formula in Figure 7. By integrating over the “resonance” interval  $m_{t\bar{t}} \in [M_{\chi_{t0}} - \Gamma, M_{\chi_{t0}} + \Gamma] = [343.43 - 2.84, 343.43 + 2.84]$  GeV, one gets the cross section of  $\sigma(pp \rightarrow \chi_{t0})_{\text{Green}} = 6.61$  fb, which is compatible with  $\sigma(pp \rightarrow \chi_{t0})_{\text{Projection}} = 10.0$  fb obtained through the projection method. Note that there is a displacement between the locations of the resonance peak predicted by the two methods, which could be due to the incomplete treatment of the  $P$ -wave Green function method adopted thus far. As demonstrated in Ref. [53], the peak location of the  $P$ -wave spectrum predicted by the Green function method depends heavily on the relative velocity (and thus momentum) between the constituents  $t$  and  $\bar{t}$ , while that of the  $S$ -wave spectrum is less sensitive, as can be seen from the results in Ref. [54]. Therefore, it is perhaps more favorable to formulate the  $P$ -wave Green function method in the momentum space, as has been proposed in Refs. [1, 5]

and carried out for the  $S$ -wave states in Ref. [14]. On top of this, Ref. [52] further points out that higher-order corrections to the  $P$ -wave Green function will induce a divergent term absent from the  $S$ -wave Green function, which, so far, cannot be dealt with using the known methods in the literature. As a result, it still remains to be explored the exact differential cross section predicted by the  $P$ -wave Green function method.

## References

- [1] V. S. Fadin and V. A. Khoze, *Threshold Behavior of Heavy Top Production in  $e^+ e^-$  Collisions*, *JETP Lett.* **46** (1987) 525–529.
- [2] J. H. Kuhn and P. M. Zerwas, *The Toponium Scenario*, *Phys. Rept.* **167** (1988) 321.
- [3] V. D. Barger, E. W. N. Glover, K. Hikasa, W.-Y. Keung, M. G. Olsson, C. J. Suchyta, III et al., *Superheavy Quarkonium Production and Decays: A New Higgs Signal*, *Phys. Rev. D* **35** (1987) 3366.
- [4] M. J. Strassler and M. E. Peskin, *The Heavy top quark threshold: QCD and the Higgs*, *Phys. Rev. D* **43** (1991) 1500–1514.
- [5] V. S. Fadin, V. A. Khoze and M. I. Kotsky, *Top quark polarization as a probe of  $t$  anti- $t$  threshold dynamics*, *Z. Phys. C* **64** (1994) 45–56, [[hep-ph/9403246](#)].
- [6] Y. Sumino, *Top quark pair production and decay near threshold in  $e^+ e^-$  collisions*, *Acta Phys. Polon. B* **28** (1997) 2461–2478, [[hep-ph/9711233](#)].
- [7] A. H. Hoang et al., *Top - anti-top pair production close to threshold: Synopsis of recent NNLO results*, *Eur. Phys. J. direct* **2** (2000) 3, [[hep-ph/0001286](#)].
- [8] K. Hagiwara, Y. Sumino and H. Yokoya, *Bound-state Effects on Top Quark Production at Hadron Colliders*, *Phys. Lett. B* **666** (2008) 71–76, [[0804.1014](#)].
- [9] Y. Sumino and H. Yokoya, *Bound-state effects on kinematical distributions of top quarks at hadron colliders*, *JHEP* **09** (2010) 034, [[1007.0075](#)].
- [10] CMS collaboration, A. Hayrapetyan et al., *Observation of a pseudoscalar excess at the top quark pair production threshold*, [2503.22382](#).
- [11] J. A. Aguilar-Saavedra, *Toponium hunter’s guide*, *Phys. Rev. D* **110** (2024) 054032, [[2407.20330](#)].
- [12] J.-H. Fu, Y.-J. Li, H.-M. Yang, Y.-B. Li, Y.-J. Zhang and C.-P. Shen, *Toponium: the smallest bound state and simplest hadron in quantum mechanics*, [2412.11254](#).
- [13] P. Nason, E. Re and L. Rottoli, *Spin Correlations in  $t\bar{t}$  Production and Decay at the LHC in QCD Perturbation Theory*, [2505.00096](#).
- [14] B. Fuks, K. Hagiwara, K. Ma and Y.-J. Zheng, *Simulating toponium formation signals at the LHC*, *Eur. Phys. J. C* **85** (2025) 157, [[2411.18962](#)].
- [15] M. Peter, *The Static quark - anti-quark potential in QCD to three loops*, *Phys. Rev. Lett.* **78** (1997) 602–605, [[hep-ph/9610209](#)].
- [16] M. Peter, *The Static potential in QCD: A Full two loop calculation*, *Nucl. Phys. B* **501** (1997) 471–494, [[hep-ph/9702245](#)].

- [17] Y. Schroder, *The Static potential in QCD to two loops*, *Phys. Lett. B* **447** (1999) 321–326, [[hep-ph/9812205](#)].
- [18] A. Vairo, *The QCD potential*, *AIP Conf. Proc.* **964** (2007) 102–109, [[0709.3341](#)].
- [19] PARTICLE DATA GROUP collaboration, S. Navas et al., *Review of particle physics*, *Phys. Rev. D* **110** (2024) 030001.
- [20] V. D. Barger and W.-Y. Keung, *Higgs Boson Production via Pseudoscalar Toponium*, *Phys. Rev. D* **37** (1988) 3172–3175.
- [21] J. Feigenbaum, *Study of toponium production including the effects of Higgs exchange*, *Phys. Rev. D* **43** (1991) 264–267.
- [22] J. H. Kuhn, *Weak Interactions of Quarkonia*, *Acta Phys. Polon. B* **12** (1981) 347.
- [23] M. Beneke, A. Signer and V. A. Smirnov, *Top quark production near threshold and the top quark mass*, *Phys. Lett. B* **454** (1999) 137–146, [[hep-ph/9903260](#)].
- [24] Y. Kats and M. D. Schwartz, *Annihilation decays of bound states at the LHC*, *JHEP* **04** (2010) 016, [[0912.0526](#)].
- [25] CMS collaboration, *Highlights of the HL-LHC physics projections by ATLAS and CMS*, [2504.00672](#).
- [26] Y. Sumino, K. Fujii, K. Hagiwara, H. Murayama and C. K. Ng, *Top quark pair production near threshold*, *Phys. Rev. D* **47** (1993) 56–81.
- [27] K. Fujii, T. Matsui and Y. Sumino, *Physics at  $t$  anti- $t$  threshold in  $e^+ e^-$  collisions*, *Phys. Rev. D* **50** (1994) 4341–4362.
- [28] T. Nagano, A. Ota and Y. Sumino,  *$O(\alpha(s)^{**2})$  corrections to  $e^+ e^- \rightarrow t$  anti- $t$  total and differential cross-sections near threshold*, *Phys. Rev. D* **60** (1999) 114014, [[hep-ph/9903498](#)].
- [29] L. D. Landau, *On the angular momentum of a system of two photons*, *Dokl. Akad. Nauk SSSR* **60** (1948) 207–209.
- [30] C.-N. Yang, *Selection Rules for the Dematerialization of a Particle Into Two Photons*, *Phys. Rev.* **77** (1950) 242–245.
- [31] CEPC STUDY GROUP collaboration, W. Abdallah et al., *CEPC Technical Design Report: Accelerator*, *Radiat. Detect. Technol. Methods* **8** (2024) 1–1105, [[2312.14363](#)].
- [32] J. Gao, *BEPCII and CEPC*, [2505.02401](#).
- [33] K. Agashe et al., *Report of the Topical Group on Top quark physics and heavy flavor production for Snowmass 2021*, [2209.11267](#).
- [34] FCC collaboration, M. Benedikt et al., *Future Circular Collider Feasibility Study Report: Volume 2, Accelerators, Technical Infrastructure and Safety*, [2505.00274](#).
- [35] FCC collaboration, M. Benedikt et al., *Future Circular Collider Feasibility Study Report: Volume 1, Physics, Experiments, Detectors*, [2505.00272](#).
- [36] Y. Koma, M. Koma and H. Wittig, *Relativistic corrections to the static potential at  $O(1/m)$  and  $O(1/m^{**2})$* , *PoS LATTICE2007* (2007) 111, [[0711.2322](#)].
- [37] T. Barnes, S. Godfrey and E. S. Swanson, *Higher charmonia*, *Phys. Rev. D* **72** (2005) 054026, [[hep-ph/0505002](#)].

- [38] J.-H. Fu, Y.-J. Zhang, G.-Z. Xu and K.-Y. Liu, *Toponium: Implementation of a toponium model in FeynRules*, [2504.12634](#).
- [39] Y. Bai and S. Westhoff, *Darkonia at colliders*, *JHEP* **04** (2025) 042, [[2412.03677](#)].
- [40] B. Fuks, *Toponium physics at the Large Hadron Collider*, May, 2025, [2505.03869](#).
- [41] L. Hostler, *Coulomb green's functions and the furry approximation*, *Journal of Mathematical Physics* **5** (05, 1964) 591–611.
- [42] CMS collaboration, A. Hayrapetyan et al., *Review of top quark mass measurements in CMS*, *Phys. Rept.* **1115** (2025) 116–218, [[2403.01313](#)].
- [43] A. D. Martin, W. J. Stirling, R. S. Thorne and G. Watt, *Parton distributions for the LHC*, *Eur. Phys. J. C* **63** (2009) 189–285, [[0901.0002](#)].
- [44] CMS collaboration, *Search for heavy pseudoscalar and scalar bosons decaying to top quark pairs in proton-proton collisions at the 13 TeV LHC*, [CMS-PAS-HIG-22-013](#).
- [45] T. Robens and T. Stefaniak, *Status of the Higgs Singlet Extension of the Standard Model after LHC Run 1*, *Eur. Phys. J. C* **75** (2015) 104, [[1501.02234](#)].
- [46] M. Carena, J. Kozaczuk, Z. Liu, T. Ou, M. J. Ramsey-Musolf, J. Shelton et al., *Probing the Electroweak Phase Transition with Exotic Higgs Decays*, *LHEP* **2023** (2023) 432, [[2203.08206](#)].
- [47] CMS collaboration, A. M. Sirunyan et al., *Measurement of the top quark Yukawa coupling from  $t\bar{t}$  kinematic distributions in the dilepton final state in proton-proton collisions at  $\sqrt{s} = 13$  TeV*, *Phys. Rev. D* **102** (2020) 092013, [[2009.07123](#)].
- [48] ATLAS collaboration, G. Aad et al., *A detailed map of Higgs boson interactions by the ATLAS experiment ten years after the discovery*, *Nature* **607** (2022) 52–59, [[2207.00092](#)].
- [49] CMS collaboration, A. Tumasyan et al., *A portrait of the Higgs boson by the CMS experiment ten years after the discovery.*, *Nature* **607** (2022) 60–68, [[2207.00043](#)].
- [50] M. Beneke, Y. Kiyo, P. Marquard, A. Penin, J. Piclum and M. Steinhauser, *Next-to-Next-to-Next-to-Leading Order QCD Prediction for the Top Antitop S-Wave Pair Production Cross Section Near Threshold in  $e^+e^-$  Annihilation*, *Phys. Rev. Lett.* **115** (2015) 192001, [[1506.06864](#)].
- [51] M. M. Defranichis, J. de Blas, A. Mehta, M. Selvaggi and M. Vos, *A detailed study on the prospects for a  $t\bar{t}$  threshold scan in  $e^+e^-$  collisions*, [2503.18713](#).
- [52] C. H. de Lima, A. Tonerio, A. Vasquez and R. Rosenfeld, *P-wave Sommerfeld enhancement near threshold: a simplified approach*, *Eur. Phys. J. C* **83** (2023) 939, [[2208.13309](#)].
- [53] R. Iengo, *Sommerfeld enhancement: General results from field theory diagrams*, *JHEP* **05** (2009) 024, [[0902.0688](#)].
- [54] M. Lattanzi and J. I. Silk, *Can the WIMP annihilation boost factor be boosted by the Sommerfeld enhancement?*, *Phys. Rev. D* **79** (2009) 083523, [[0812.0360](#)].